2D Materials

RECEIVED
4 November 2018

REVISED
17 January 2019

ACCEPTED FOR PUBLICATION
14 February 2019

PUBLISHED
15 March 2019

PAPER

Strongly tunable anisotropic thermal transport in MoS_2 by strain and lithium intercalation: first-principles calculations

Shunda Chen[1], Aditya Sood[2,3,6], Eric Pop[2,4,5], Kenneth E Goodson[3] and Davide Donadio[1]

[1] Department of Chemistry, University of California Davis, One Shields Ave. Davis, CA 95616, United States of America
[2] Department of Electrical Engineering, Stanford University, Stanford, CA 94305, United States of America
[3] Department of Mechanical Engineering, Stanford University, Stanford, CA 94305, United States of America
[4] Department of Materials Science and Engineering, Stanford University, Stanford, CA 94305, United States of America
[5] Precourt Institute for Energy, Stanford University, Stanford, CA 94305, United States of America
[6] Present address: Stanford Institute for Materials and Energy Sciences, SLAC National Accelerator Laboratory, Menlo Park, CA 94025, United States of America

E-mail: shdchen@ucdavis.edu and ddonadio@ucdavis.edu

Keywords: thermal conductivity, intercalation, molybdenum disulphide, strain

Supplementary material for this article is available online

Abstract

The possibility of tuning the vibrational properties and the thermal conductivity of layered van der Waals materials either chemically or mechanically paves the way to significant advances in nanoscale heat management. Using first-principles calculations we investigate the modulation of heat transport in MoS_2 by lithium intercalation and cross-plane strain. We find that both the in-plane and cross-plane thermal conductivity (κ_r, κ_z) of MoS_2 are extremely sensitive to both strain and electrochemical intercalation. Combining lithium intercalation and strain, the in-plane and cross-plane thermal conductivity can be tuned over one and two orders of magnitude, respectively. Furthermore, since κ_r and κ_z respond in different ways to intercalation and strain, the thermal conductivity anisotropy can be modulated by two orders of magnitude. The underlying mechanisms for such large tunability of the anisotropic thermal conductivity of MoS_2 are explored by computing and analyzing the dispersion relations, group velocities, relaxation times and mean free paths of phonons. Since both intercalation and strain can be applied reversibly, their stark effect on thermal conductivity can be exploited to design novel phononic devices, as well as for thermal management in MoS_2-based electronic and optoelectronic systems.

1. Introduction

Among two-dimensional (2D) layered materials, transition metal dichalcogenides (TMDCs) are of special interest for next-generation electronic and optoelectronic devices. In fact, in contrast to graphene, many TMDCs are semiconductors with considerable band gap [1–4]. Among TMDCs, molybdenum disulphide (MoS_2) has been explored most intensively [2–10]. Its mechanical flexibility makes it a compelling semiconducting material for flexible electronics [11–14], and its large interlayer separation provides ideal space to intercalate guest species, such as alkali metal ions. Lithium intercalation of MoS_2, has been reported to enhance the optical transmission and increase electrical conductivity due to changes in the electronic band structure and the injection of free carriers [15]. Reversible intercalation and deintercalation of Li in MoS_2 opens a route for novel applications in batteries and supercapacitors [16].

Thermal management in such applications, both at the nanoscale and at the macroscopic scale is a crucial issue [17]. As in other layered van der Waals materials, heat transport in MoS_2 is strongly anisotropic, featuring high thermal conductivity in plane and low conductivity across the layers. In spite of its importance, the estimates of thermal conductivity of MoS_2 reported are in a wide range. The experimental estimates for in-plane thermal conductivity (κ_r) at room temperature vary from 13.3 to 110 $Wm^{-1} K^{-1}$ [18–24], and those of cross-plane thermal conductivity (κ_z) vary from 2.0 to 5.3 $Wm^{-1} K^{-1}$ [21, 24, 25]. Such discrepancies may stem either from different quality of samples or from different experimental conditions and measurement techniques.

Even though it was suggested that intercalation may produce substantial reduction of thermal conductivity [14, 26], fundamental aspects of thermal transport in intercalated MoS_2 are still not well understood. Recent measurements indicate that lithiation reduces κ_z of a vertically aligned MoS_2 thin-film by a factor of two, while the effect on bulk samples is non-monotonic as a function of the concentration of Li [27]. At a fractional Li composition x (in Li_xMoS_2) of 0.86, κ_z of bulk MoS_2 is reduced by 1.25 times, and κ_r is reduced by about 1.31 times [27]. In addition, thermal conductance across tens of nanometer thick MoS_2 films can be reversibly reduced by up to $\sim$10 times through electrochemical lithiation [28].

Atomistic simulations could provide a rationale for such experimental findings, and help to resolve discrepancies in experiments. Heat transport in MoS_2 has been addressed theoretically by both first-principles anharmonic lattice dynamics and molecular dynamics (MD) simulations. First-principles calculations can be transferable and predictive, but the computation of anharmonic force constants and the solution of the linearized Boltzmann transport equation (BTE) need to satisfy tight convergence criteria. Former first-principles BTE calculations give κ_r between 83–103 Wm^{-1} K^{-1} [29–31], and κ_z from 2.3 to 5.1 Wm^{-1} K^{-1} [29–31]. Non-monotonic changes of κ as a function of partial lithium intercalation were recently reproduced by first-principles calculations on finite thickness open systems [32]. MD simulations, in turn, depend on the quality of the empirical potentials utilized, and provide too large a range of estimates for κ_r from 1.35 to 531 Wm^{-1} K^{-1} [33–39], whereas for κ_z values are between 2.0 and 6.6 Wm^{-1} K^{-1} [33, 39, 40]. Interestingly, MD simulations predicted a large modulation of κ_z as a function of cross-plane strain [37], but it is necessary to verify whether this result is independent of the adopted empirical potential in order to provide quantitative predictions that would aid the design of new MoS_2-based materials and devices.

While the possibility of modulating the thermal conductivity of MoS_2 is very appealing for applications in nanoscale electronic and thermal devices with tunable thermal functionality [25, 41–51], a compelling understanding of the combined effects of strain and electrochemical intercalation is still lacking.

To fill this gap, we investigate the phonon properties and thermal conductivity of pristine and lithiated MoS_2 ($LiMoS_2$), and we systematically probe the influence of cross-plane strain effects, by first-principles calculations. We show that both the in-plane and cross-plane thermal conductivity of MoS_2 can be tuned substantially by lithium intercalation and cross-plane strain. For both pristine MoS_2 and $LiMoS_2$, the cross-plane thermal conductivity is strongly enhanced by compressive strain and decreased by tensile strain. In MoS_2 such variation amounts to up to two orders of magnitude for the strain range investigated. Furthermore we show that Li intercalation produces a more than seven-fold reduction of κ_r, while κ_z is halved. The different response of the in-plane and cross-plane components of κ may be exploited to modulate the anisotropy ratio, so to achieve more or less directional heat dissipation.

We compute the thermal conductivity of pristine hexagonal trigonal prismatic (2H)-MoS_2 and $LiMoS_2$ by solving the linearized phonon BTE, with harmonic and anharmonic force constants computed by first-principles density functional theory (DFT). DFT calculations are performed using both the local density approximation (LDA) and a van der Waals functional (vdW-DF) with consistent exchange (vdW-DF-cx) [52]. This first-principles BTE (FP-BTE) approach [53] has proven accurate and predictive for a large variety of systems, including 2D and van der Waals layered materials [31, 54–62]. As a result of linearizing and solving the BTE, the lattice thermal conductivity tensor κ is expressed as:

$$\kappa_{\alpha\beta} = \frac{1}{V}\sum_{\lambda}\hbar\omega_{\lambda}\frac{\partial f}{\partial T}v_{\lambda}^{\alpha}v_{\lambda}^{\beta}\tau_{\lambda}^{\beta}, \quad (1)$$

where f is the Bose–Einstein distribution function, ω_λ is the phonon angular frequency, $v_\lambda^{\alpha(\beta)}$ is the group velocity component along the $\alpha(\beta)$-direction, and τ_λ^β is the relaxation time for phonons with polarization λ propagating in the direction β. Self-consistent (SCF) BTE entails a directional dependence of phonon relaxation times, as the direction of the heat flux determines different shifts in the phonon population and therefore different scattering efficiency [54, 62]. In the calculation of phonon relaxation times we consider intrinsic three-phonon scattering processes and extrinsic isotopic mass scattering [63]. The natural isotopic distributions of Mo, S, and Li are considered [64] and results are compared to those obtained for isotopically pure systems, to assess the effect of isotopic scattering. Systems are considered in the infinite periodic bulk limit with no boundary scattering.

Following equation (1), FP-BTE not only provides a reliable estimate of κ, but it also allows one to resolve the contribution to κ in terms of phonon frequency, polarization and mean free path (MFP), thus uncovering the mechanistic details of heat transport in crystalline materials. Our accurate, well converged, parameter-free first-principles calculations predict a strong modulation of thermal conductivity of layered MoS_2 by mechanical strain and lithium intercalation, and provide both a detailed microscopic interpretation of recent experiments and reliable benchmarks for future ones.

2. Results and discussion

2.1. Structure

The stable 2H phase of MoS_2 consists of planes with one formula unit each per unit cell, arranged in AB stacking. Upon lithium intercalation, MoS_2 planes undergo a transition from trigonal prismatic 2H to distorted octahedral 1T, and their stacking changes from AB to AA [68]. The in-plane symmetry is reduced

Table 1. Equilibrium lattice parameters (in units of Angstrom) of pristine (2H)-MoS_2 and (1T)-$LiMoS_2$.

Method	(2H)-MoS_2		(1T)-$LiMoS_2$		*a*-axis expansion (%)	*c*-axis expansion (%)
	a	*c*	*a*	*c*		
LDA (This work)	3.142	12.053	6.776	6.054	7.8	0.46
vdW-DF-cx (This work)	3.158	12.284	6.789	6.229	7.5	1.4
LDA ([30])	3.14	12.05	—	—	—	—
PBE (DFT-D3) ([29])	3.157	12.225	—	—	—	—
vdW-DF-cx ([31])	3.152	12.291	—	—	—	—
Exp. ([65])	3.168	12.322	—	—	—	—
Exp. ([66])	—	—	6.798	6.262	7.3	1.6
Exp. ([27])	—	12.32	—	6.19	—	0.5

and in the 1T phase the primitive cell contains four $LiMoS_2$ units in a 2×2 superstructure.

The optimized lattice parameters of both pristine and lithiated MoS_2 (table 1) compare very well with experiments. These results confirm that our computational framework accurately describes the structural features of MoS_2 and their changes upon Li intercalation. In particular, we note that the 2H to 1T transition, occurring upon intercalation, produces an expansion of the in-plane lattice parameter by 7.8% [66], but accommodates lithium with an inter-planar expansion as small as 0.5%, as also observed in recent experiments [27]. vdW-DF-cx calculations give lattice constants closer to experiments (within 0.4%) than LDA, and consistent lattice expansion rates: *a*-axis (in-plane) expansion of 7.5% and *c*-axis (cross-plane) expansion of 1.4%, which are in good agreement with experimental data [66]. This result is important, because it suggests that in experiments, in which large *c*-axis expansion rates are observed [69–71], either the transition to the 1T phase is not complete or samples entail mesoscale disorder that induces strain.

Upon intercalation Li donates an electron to the system, which would in principle become metallic. However a Jahn–Teller transition [72] to the distorted 1T phase re-instates a gap between the valence and conduction band, making the system a semiconductor. Even if the 1T lithiated system were assumed to be metallic, the electrical contribution to thermal conductivity would be much smaller than the lattice contribution, as estimated by Zhu *et al* [27]. Hence, in the following we can safely neglect the contribution of electrons to thermal transport.

2.2. Thermal conductivity

Figure 1 shows the in-plane and cross-plane thermal conductivity of pristine and fully lithiated MoS_2 as a function of strain. Since the discrepancies among former FP-BTE calculations [29–31] of the thermal conductivity of pure MoS_2 may be due to convergence issues, we have taken care of converging our calculations with respect to all the DFT and BTE parameters (see supplementary figures S1–S13 (stacks.iop.org/TDM/6/025033/mmedia)). In particular, due to the long-range nature of the interactions in MoS_2, it is critical to consider interactions up to the 9th neighbors shell to construct the anharmonic force constants tensor in order to achieve well-converged results for κ (figure S7).

We find that isotopic scattering has a strong effect on κ_r, for which isotopically pure MoS_2 turns out about 20% higher than that of MoS_2 with natural composition. The isotopic effect for κ_z is milder as the difference is only 10%, and it is even weaker on both κ_r and κ_z of $LiMoS_2$ (see figures 1 and S25 for more details). The following results refer to materials with natural isotopic composition.

Along with structural changes, lithium intercalation into MoS_2 leads to a seven-fold reduction of in-plane thermal conductivity, and two-fold reduction in cross-plane thermal conductivity. The two-fold reduction in κ_z upon full lithiation predicted by FP-BTE is on the same order as the reduction of κ_z measured by Zhu *et al* [27] for bulk MoS_2 (the measured κ_z drops from $\sim$2 to $\sim$1.6 Wm^{-1} K^{-1} upon lithiation to $x = 0.86$, a factor of $\sim$1.25). Note that our FP-BTE predicts κ_z of pristine bulk MoS_2 of about $\sim$5 Wm^{-1} K^{-1}, whereas Zhu *et al* [27] measured $\sim$2 Wm^{-1} K^{-1}. Such discrepancy may be due to the small penetration depth (high modulation frequency) of the time-domain thermoreflectance (TDTR) measurement, as discussed in [24, 67, 73]. However, given that the source of MoS_2 crystals is generally mineralogical, variations in crystal quality between samples cannot entirely be ruled out. Our results set the theory benchmark for the thermal conductivity of an unlithiated pristine system, and are in excellent agreement with recent measurements by Jiang *et al* [24, 67] and DFT calculations by Lindroth *et al* [31]. As for in-plane thermal conductivity there is a striking discrepancy between calculations and TDTR measurements [27], which suggest that κ_r is only slightly affected by lithium intercalation. Such discrepancy between *ab initio* theory and experiments would deserve further investigation.

Even larger modulations of κ occur in samples strained in the direction perpendicular to the MoS_2 planes. In these calculations the cross-plane lattice parameter c is fixed and all the other parameters,

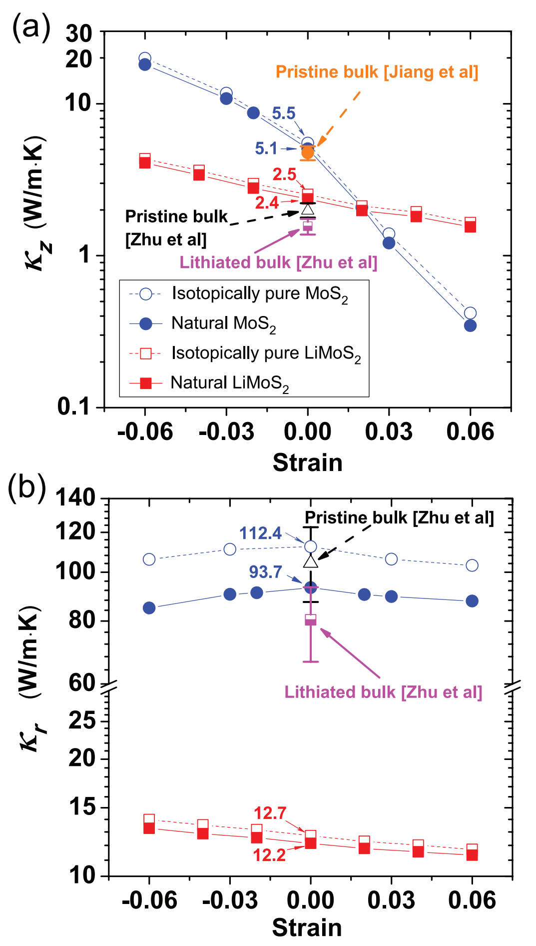

Figure 1. Calculated cross-plane (a) and in-plane (b) thermal conductivity as a function of cross-plane strain for pristine MoS_2 (blue open circles for isotopically pure MoS_2, blue full circles for natural MoS_2) and $LiMoS_2$ (red open squares for isotopically pure $LiMoS_2$, red full squares for natural $LiMoS_2$), also showing measurements from Zhu *et al* [27] and Jiang *et al* [24, 67].

including the in-plane lattice parameter a are relaxed. We consider strain (ε) from -6% (compressive) to 6% (tensile), corresponding to applied stress from -6 to 5 GPa, respectively (figure S14). The cross-plane thermal conductivity of pristine MoS_2 varies monotonically over two orders of magnitude, from 0.35 Wm^{-1} K^{-1} upon 6% tensile strain to 18.09 Wm^{-1} K^{-1} upon 6% compressive strain. Recent measurements show that κ_z increases under compressive strain in multilayer MoS_2 [74], in qualitative agreement with our predictions. In contrast, the cross-plane thermal conductivity of $LiMoS_2$ exhibits less variability, from 1.5 Wm^{-1} K^{-1} upon 6% tensile strain to 4.1 Wm^{-1} K^{-1} upon 6% compressive strain. Consequently, a crossover in κ_z occurs upon tensile strain: the cross-plane thermal conductivity of $LiMoS_2$ becomes larger than that of MoS_2 for tensile strain larger than 2%. Cross-plane strain also causes variations of the in-plane thermal conductivity but to a lesser extent. κ_r of MoS_2 is reduced by up to about 10% by either tensile or compressive strain. κ_r of $LiMoS_2$ varies monotonically from 11.3 Wm^{-1} K^{-1} for systems subject to large tensile strain to 13.3 Wm^{-1} K^{-1} upon compressive strain.

Since cross-plane and in-plane components of the thermal conductivity tensor show different sensitivity to cross-plane strain, it is then possible to modulate the anisotropy ratio (κ_r/κ_z) over a very wide range of values. Within the strain range investigated, the anisotropy ratio of MoS_2 is varied from $\sim$5 to $\sim$250 (figure 2). Conversely, lithiation significantly reduces the overall anisotropy of κ and the ratio κ_r/κ_z changes from 3.3 to 7.3 as a function of strain. The modulation of the anisotropy ratio of κ is not significantly affected by isotopic composition.

2.3. Phonon properties

We now analyze the origin of the modulation of thermal conductivity induced by lithium intercalation and strain, in terms of phonon properties and their contribution to κ, as expressed by equation (1). The two panels of figure 3 display the effects of Li intercalation and strain on phonon dispersion relations. Previous reports showed that the majority heat carriers are acoustic modes with frequency below 6 THz for in-plane and 3 THz for cross-plane (see also figure 6), and that the gap between acoustic and optical modes in pure MoS_2 limits the amount of viable scattering channels, leading to very high in-plane thermal conductivity [29–31].

Upon intercalation we observe two major changes in the dispersion relations. On the one hand, both in-plane and cross-plane acoustic modes are stiffened upon lithiation. On the other hand the larger number of atoms per unit cell in $LiMoS_2$ engenders a corresponding number of phonon branches that fill the gaps of the spectrum of MoS_2 (see figures 3, S12, S13 and S15). The majority of these optical modes, especially those localized on Li atoms have relatively flat dispersion and do not carry significant amounts of heat, but they contribute scattering channels to acoustic modes [28]. The overall effect is a significant reduction of κ, especially in-plane.

Cross-plane strain mostly influences the dispersion relations of the acoustic modes of both MoS_2 and $LiMoS_2$. Along the Γ–A high symmetry direction, i.e. cross-plane, compressive strain induces a significant stiffening of all three acoustic branches in both systems, while tensile strain induces softening. For phonons propagating in-plane (Γ–M–K–Γ path), cross-plane strain impacts only the flexural modes, producing either stiffening (compressive) or softening (tensile).

The magnitude of such changes is much larger for MoS_2 than for $LiMoS_2$, as confirmed by the calculation of the cross-plane group velocities, reported in figures 4(a) and (d). The group velocities of the phonons propagating across the layers of MoS_2 are largely enhanced upon compression and reduced upon tensile strain, in accordance with the effect seen on its thermal conductivity. In particular, the speed of sound increases from 3000 m s^{-1} to 5500 m s^{-1} upon 6% compression. Considering that acoustic modes are

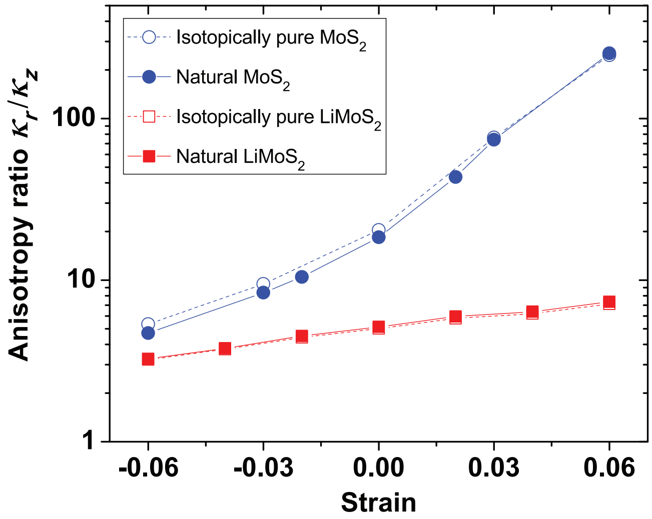

Figure 2. Anisotropy ratio of in-plane thermal conductivity κ_r to cross-plane thermal conductivity κ_z as a function of cross-plane strain for pristine MoS_2 (blue open circles for isotopically pure MoS_2, blue full circles for natural MoS_2) and $LiMoS_2$ (red open squares for isotopically pure $LiMoS_2$, red full squares for natural $LiMoS_2$). The stress corresponding to the strain considered is reported in figure S14.

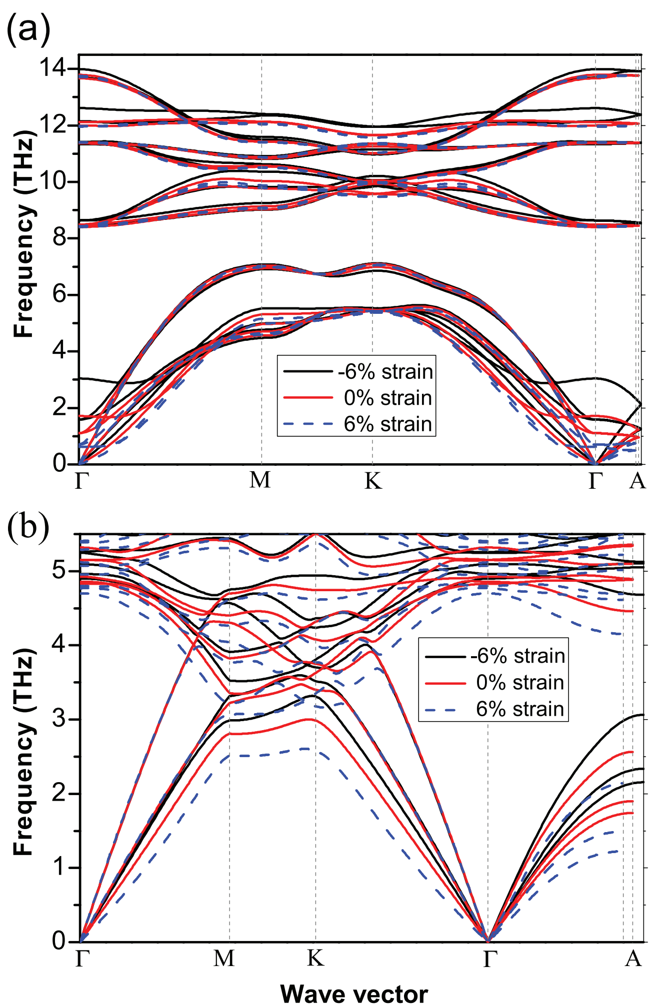

Figure 3. Phonon dispersion relations for (a) MoS_2 and (b) $LiMoS_2$, under -6% (black lines), 0% (red lines), and 6% strain (blue dashed lines).

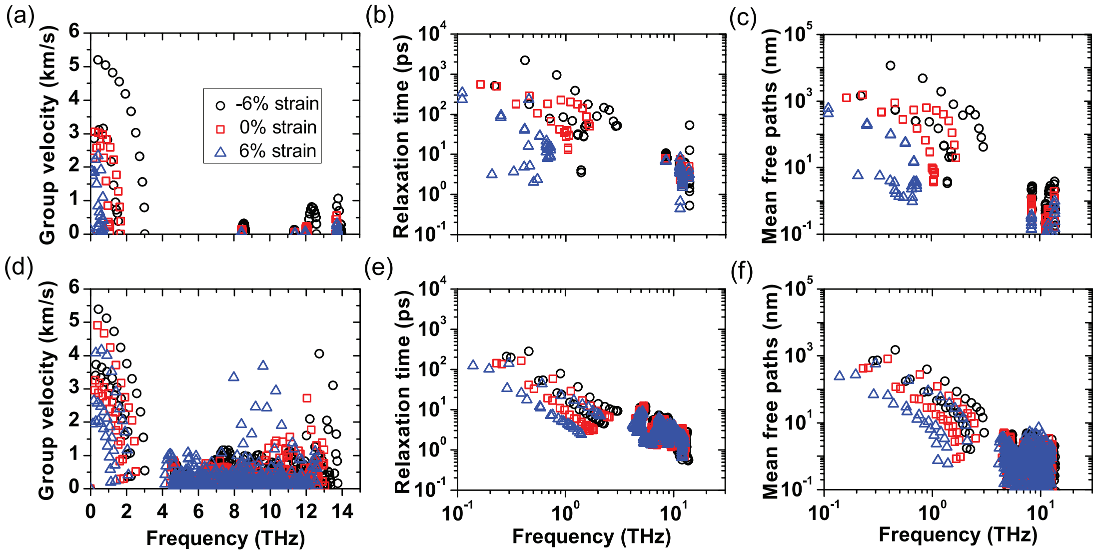

Figure 4. (a)–(c) Phonon group velocity, relaxation time, and mean free paths along Γ–A (cross-plane) direction for pristine MoS_2 under −6% (black circles), 0% (red squares), and 6% strain (blue triangles); (d)–(f) the same but for $LiMoS_2$.

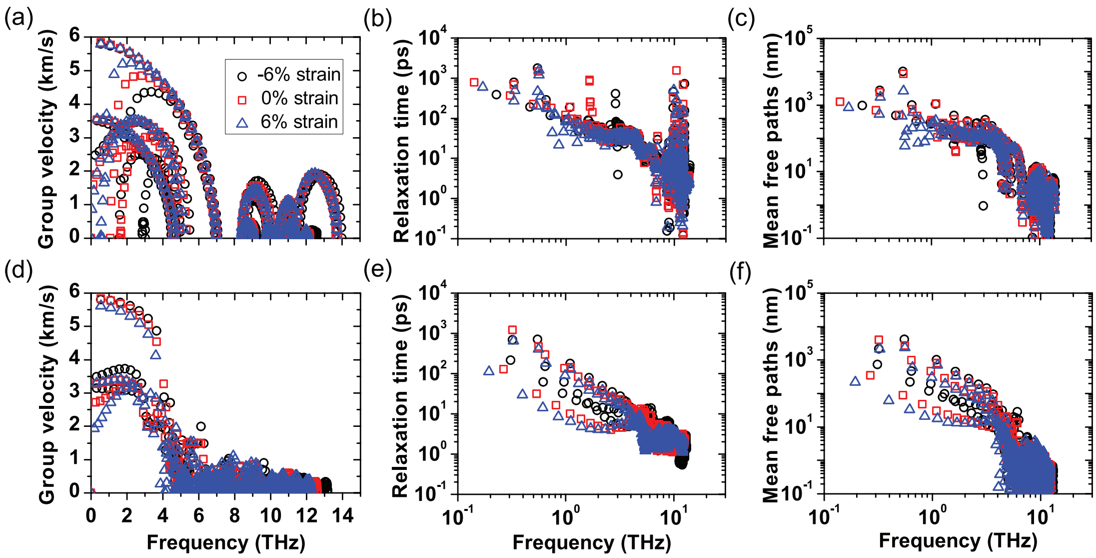

Figure 5. (a)–(c) Phonon group velocity, relaxation time, and mean free paths along Γ–M (in-plane) direction for pristine MoS_2 under −6% (black circles), 0% (red squares), and 6% strain (blue triangles); (d)–(f) the same but for $LiMoS_2$.

the main heat carriers, and that κ is proportional to v^2, such change is sufficient to justify the increase of thermal conductivity upon compression from ∼5 to ∼18 Wm^{-1} K^{-1} (figure 1(a)). The same argument explains the reduction of κ_z upon tensile strain.

Such variations of group velocities are accompanied by enhancement/reduction in phonon relaxation times (figure 4(b)), hence in mean free paths (figure 4(c)), which overall contribute to the observed strong modulation of κ. In $LiMoS_2$, group velocities, relaxation times and mean free paths follow the same trends as in MoS_2, but the effect of strain is much weaker (figures 4(d)–(f)). This occurs because the stiffening of the structure upon intercalation limits the range of variation of the cross-plane group velocities. For compressed and unstrained systems, phonon lifetimes in $LiMoS_2$ are significantly smaller than those in pristine MoS_2, resulting in a much reduced κ_z. However, the smaller range of variation of group velocities and lifetimes upon tensile strain leads to the observed crossover in κ_z at 2% strain. Hence intercalated ions may play a role as channels between layers, possibly enhancing heat transport in weakly bonded strained systems.

The analysis of the in-plane phonon properties of MoS_2 and $LiMoS_2$ sheds light on the trends of κ_r. Group velocities, relaxation times and mean free paths along the high symmetry Γ–M direction are reported in figures 5(a)–(c) for pristine MoS_2 and figures 5(d)–(f) for $LiMoS_2$. The effect of lithium intercalation on in-plane phonon modes is to reduce the frequency range of acoustic modes with significant group velocity, as well as to reduce the overall lifetimes and mean free paths. Both these effects are consequences of the 2H–1T structural transition, and account for the observed

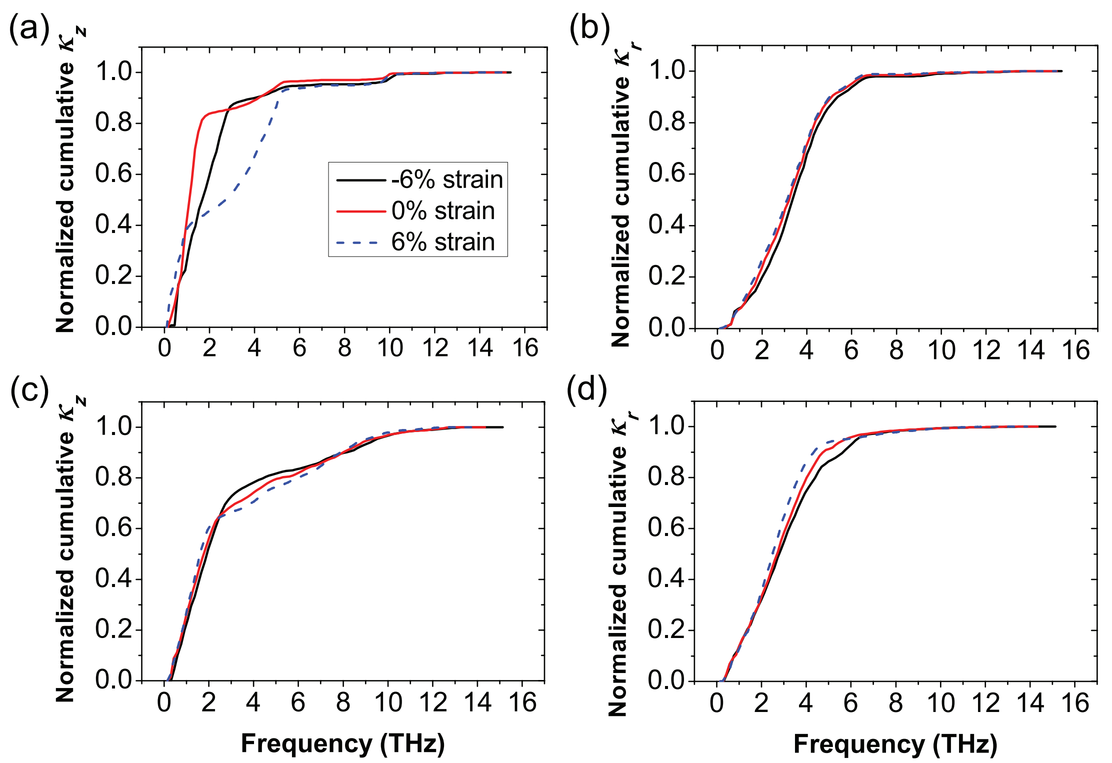

Figure 6. Normalized frequency-dependent cumulative cross-plane (a) and and in-plane (b) thermal conductivity for pristine MoS_2 under −6% (black line), 0% (red line), and 6% strain (blue dashed line); (c) and (d) the same but for $LiMoS_2$.

major reduction of κ_r from 93.7 to 12.2 Wm^{-1} K^{-1}. For pristine MoS_2, strain reduces the MFPs of the ZA modes through two different mechanisms. Compressive strain reduces the group velocities, whereas tensile strain reduces the relaxation times. These two disparate effects cause a mild reduction of κ_r upon both tensile and compressive cross-plane strain, inducing the non-monotonic behavior shown in figure 1(b). For $LiMoS_2$, both the group velocities and the relaxation times of the ZA modes increase upon compressive deformations and decrease under tensile strain, leading to a monotonic trend of κ_r versus strain.

These effects modify the relative contribution of phonons with different frequency to the total cross-plane and in-plane thermal conductivity, as shown by the cumulative κ_r and κ_z as a function of frequency reported in figure 6. For pristine MoS_2, compressive strain extends the contribution of higher frequencies to κ_z by stiffening of the acoustic branches. Conversely, tensile strain reduces the range of the acoustic branches so much that the relative contribution of higher frequencies appears more relevant. Li intercalation extends substantially the range of frequencies that contribute to cross-plane heat transport, making the contributions from optical modes up to ~11 THz relevant. As for in-plane heat transport, Li intercalation significantly affects the absolute value of κ_r, but not the relative contribution of different phonon frequencies. The relative contribution of different phonon frequencies to κ_r is mildly affected for the lightly stiffening (softening) of flexural modes by compressive (tensile) strain.

Although we have not considered the effect of in-plane strain, we argue that it would induce the modulation of phonon transport analogous to those computed upon cross-plane strain, due to the mechanical response of the system through its Poisson's ratio (figures S26 and S27) [75–77]. Consistent with this argument, MD simulations suggested that both tensile and compressive in-plane strain would reduce κ_r of single-layer MoS_2 [78].

3. Conclusions

In conclusion, first-principles calculations performed with strict convergence criteria allow us to resolve discrepancies in the literature about the thermal conductivity of bulk MoS_2, thus establishing a reliable benchmark for future experiments and simulations.

These calculations show that both the in-plane and cross-plane thermal conductivity of MoS_2 are critically sensitive to both strain and intercalation. We predict that lithium intercalation of bulk MoS_2 produces more than seven-fold reduction in κ_r, and two-fold reduction in κ_z. These results constitute a lower bound for the thermal conductivity modulation caused by Li intercalation, without considering structural disorder (mixed phases, vacancies, etc). Most remarkably, κ_z of MoS_2 can be modulated over two orders of magnitude by strain between −6% to 6%, whereas κ_z of $LiMoS_2$ is less sensitive to strain. By combining strain and intercalation it is possible to tune the anisotropy ratio of κ from 5 to 250. Being able to modulate the thermal conductivity anisotropy ratio over such a wide range can have important applications in thermal management. These calculations provide a theoretical benchmark that will enable the interpretation of experimental measurements of thermal conduction in intercalated van der Waals transition metal dichalcogenides. They provide guidelines to design materials and engineer devices with tunable thermal conductivity.

4. Methods

To properly take into account collective effects in phonon transport, we solve the BTE self-consistently, as implemented in the ShengBTE code [54, 79–81].

DFT calculations are performed within LDA of the exchange and correlation functional [82] by using the quantum-espresso package [83, 84]. Core electrons are approximated using norm-conserving pseudopotentials [85], and the valence electronic wavefunctions are expanded in a plane-wave basis set with a kinetic energy cutoff of 100 Ry. The charge density is integrated on $10 \times 10 \times 4$ and $4 \times 4 \times 4$ Monkhorst–Pack meshes of k-points for pristine MoS_2 and $LiMoS_2$, respectively. Structural and cell relaxations are performed using a quasi-Newton optimization algorithm with a tight convergence criterion of 10^{-8} Rydberg/Bohr for maximum residual force component. To model lithium intercalation of MoS_2, we used the optimized MoS_2 structure to construct a $2 \times 2 \times 1$ supercell, and inserted Li atoms in the vdW gap. We verified that the system relaxes spontaneously to the distorted 1T phase.

We utilize density-functional perturbation theory (DFPT) [86] to calculate harmonic interatomic force constants (IFCs) with $10 \times 10 \times 4$ and $4 \times 4 \times 4$ q-point meshes for pristine (2H)-MoS_2 and $LiMoS_2$, respectively. Anharmonic third order force constants for the calculation of lattice thermal conductivity are computed by finite differences up to a cutoff interatomic distance 7.04 Å, corresponding to the 11th nearest neighbour shell, in a $5 \times 5 \times 1$ supercell containing 150 atoms for pristine (2H)-MoS_2. For (1T)-$LiMoS_2$ we use a cutoff up to 8th nearest neighbour in a $2 \times 2 \times 2$ super-cell with 128 atoms. Third derivatives of the potential energy with respect to displacements of atoms ijk along $\alpha\beta\gamma$ coordinates are computed by finite differences ($\delta x = 0.01$ Å), and translational invariance is enforced using the Lagrangian approach [81].

For pristine MoS_2, it is necessary to take iterative SCF calculations, since relaxation time approximation (RTA) underestimates its thermal conductivity (see figures S16 and S17). For $LiMoS_2$, we found that RTA yields the same results as SCF within 1% (see figures S18 and S19). We carefully checked the convergence with q-points grids up to $45 \times 45 \times 11$ for pristine MoS_2 (see figure S5) and up to $23 \times 23 \times 23$ for $LiMoS_2$ (see figure S6). Details on convergence tests are provided in the supporting information.

The main results of this work are confirmed by calculations performed using a van der Waals density functional (vdW-DF) [87–90] with non-empirical consistent exchange (vdW-DF-cx) [52, 91], and projector augmented wave (PAW) pseudopotentials [92, 93] (see figures S20–S24). These tests justify *a posteriori* the use of LDA, which reproduces the van der Waals interaction among different planes due to error cancellation between the exchange and the correlation parts of the functional, and our calculated phonon dispersion relations of MoS2 are in very good agreement with experimental data [94, 95]. More details are provided in the supporting information.

Acknowledgments

Useful discussions with Jesús Carrete, Wu Li, Majid Zeraati, David Strubbe, Daniele Selli and Shruba Ganghopadhyay are gratefully acknowledged. AS, EP and KEG acknowledge funding from the National Science Foundation (NSF) under the EFRI 2-DARE grant 1542883 and from the Stanford SystemX Alliance.

Supporting information

Detailed convergence tests of FP-BTE calculations, full phonon dispersion curves, stress–strain curves for pristine MoS_2 and $LiMoS_2$ (figures S1–S15); comparison between the SCF solution and RTA of the BTE (figures S16–S19); calculations performed using van der Waals density functional (vdW-DF, with non-empirical consistent exchange) and PAW pseudopotentials (figures S20–S24); a comparison of κ of systems with isotopically pure and natural isotopic composition upon cross-plane strain (figure S25); the Poisson's ratio for pristine MoS_2 and $LiMoS_2$ by LDA and vdW-DF with non-empirical consistent exchange (figures S26 and S27).

ORCID iDs

Shunda Chen https://orcid.org/0000-0002-5506-7507
Aditya Sood https://orcid.org/0000-0002-4319-666X
Eric Pop https://orcid.org/0000-0003-0436-8534
Davide Donadio https://orcid.org/0000-0002-2150-4182

References

[1] Chhowalla M, Shin H S, Eda G, Li L J, Loh K P and Zhang H 2013 *Nat. Chem.* **5** 263–75
[2] Wang Q H, Kalantar-Zadeh K, Kis A, Coleman J N and Strano M S 2012 *Nat. Nanotechnol.* **7** 699–712
[3] Butler S Z *et al* 2013 *ACS Nano* **7** 2898–926
[4] Duong D L, Yun S J and Lee Y H 2017 *ACS Nano* **11** 11803–30
[5] Splendiani A, Sun L, Zhang Y, Li T, Kim J, Chim C Y, Galli G and Wang F 2010 *Nano Lett.* **10** 1271–5
[6] Smithe K K H, English C D, Suryavanshi S V and Pop E 2017 *2D Mater.* **4** 011009
[7] Sundaram R S, Engel M, Lombardo A, Krupke R, Ferrari A C, Avouris P and Steiner M 2013 *Nano Lett.* **13** 1416–21

[8] Lee H S, Min S W, Chang Y G, Park M K, Nam T, Kim H, Kim J H, Ryu S and Im S 2012 *Nano Lett.* **12** 3695–700
[9] Yin Z, Li H, Li H, Jiang L, Shi Y, Sun Y, Lu G, Zhang Q, Chen X and Zhang H 2012 *ACS Nano* **6** 74–80
[10] Tsai M L, Su S H, Chang J K, Tsai D S, Chen C H, Wu C I, Li L J, Chen L J and He J H 2014 *ACS Nano* **8** 8317–22
[11] Pu J, Yomogida Y, Liu K K, Li L J, Iwasa Y and Takenobu T 2012 *Nano Lett.* **12** 4013–7
[12] Chang H Y, Yang S, Lee J, Tao L, Hwang W S, Jena D, Lu N and Akinwande D 2013 *ACS Nano* **7** 5446–52
[13] Cheng R, Jiang S, Chen Y, Liu Y, Weiss N, Cheng H C, Wu H, Huang Y and Duan X 2014 *Nat. Commun.* **5** 5143
[14] Wan C *et al* 2015 *Nat. Mater.* **14** 622–7
[15] Xiong F, Wang H, Liu X, Sun J, Brongersma M, Pop E and Cui Y 2015 *Nano Lett.* **15** 6777–84
[16] Rasamani K D, Alimohammadi F and Sun Y 2017 *Mater. Today* **20** 83–91
[17] Pop E 2010 *Nano Res.* **3** 147–69
[18] Sahoo S, Gaur A P S, Ahmadi M, Guinel M J F and Katiyar R S 2013 *J. Phys. Chem.* C **117** 9042–7
[19] Yan R, Simpson J R, Bertolazzi S, Brivio J, Watson M, Wu X, Kis A, Luo T, Hight Walker A R and Xing H G 2014 *ACS Nano* **8** 986–93
[20] Jo I, Pettes M T, Ou E, Wu W and Shi L 2014 *Appl. Phys. Lett.* **104** 201902
[21] Liu J, Choi G M and Cahill D G 2014 *J. Appl. Phys.* **116** 233107
[22] Zhang X, Sun D, Li Y, Lee G H, Cui X, Chenet D, You Y, Heinz T F and Hone J C 2015 *ACS Appl. Mater. Interfaces* **7** 25923–9
[23] Bae J J, Jeong H Y, Han G H, Kim J, Kim H, Kim M S, Moon B H, Lim S C and Lee Y H 2017 *Nanoscale* **9** 2541–7
[24] Jiang P, Qian X and Yang R 2017 *Rev. Sci. Instrum.* **88** 074901
[25] Muratore C, Varshney V, Gengler J J, Hu J, Bultman J E, Roy A K, Farmer B L and Voevodin A A 2014 *Phys. Chem. Chem. Phys.* **16** 1008–14
[26] Cho J, Losego M D, Zhang H G, Kim H, Zuo J, Petrov I, Cahill D G and Braun P V 2014 *Nat. Commun.* **5** 4035
[27] Zhu G, Liu J, Zheng Q, Zhang R, Li D, Banerjee D and Cahill D G 2016 *Nat. Commun.* **7** 13211
[28] Sood A *et al* 2018 *Nat. Commun.* **9** 4510
[29] Gandi A N and Schwingenschlögl U 2016 *Europhys. Lett.* **113** 36002
[30] Gu X, Li B and Yang R 2016 *J. Appl. Phys.* **119** 085106
[31] Lindroth D O and Erhart P 2016 *Phys. Rev.* B **94** 115205
[32] Bunjaku T and Luisier M 2018 (arXiv:1811.07695 [cond-mat])
[33] Varshney V, Patnaik S S, Muratore C, Roy A K, Voevodin A A and Farmer B L 2010 *Comput. Mater. Sci.* **48** 101–8
[34] Liu X, Zhang G, Pei Q X and Zhang Y W 2013 *Appl. Phys. Lett.* **103** 133113
[35] Jiang J W, Park H S and Rabczuk T 2013 *J. Appl. Phys.* **114** 064307
[36] Wei X, Wang Y, Shen Y, Xie G, Xiao H, Zhong J and Zhang G 2014 *Appl. Phys. Lett.* **105** 103902
[37] Ding Z, Jiang J W, Pei Q X and Zhang Y W 2015 *Nanotechnology* **26** 065703
[38] Kandemir A, Yapicioglu H, Kinaci A, Çağın T and Sevik C 2016 *Nanotechnology* **27** 055703
[39] Xu K *et al* 2019 *Phys. Rev.* B **99** 054303
[40] Wei Z, Liu B, Liu C, Bi K, Yang J and Chen Y 2015 *J. Phys. D: Appl. Phys.* **48** 465303
[41] Cahill D G *et al* 2014 *Appl. Phys. Rev.* **1** 011305
[42] Wang H, Yuan H, Hong S S, Li Y and Cui Y 2015 *Chem. Soc. Rev.* **44** 2664–80
[43] Chiritescu C, Cahill D G, Nguyen N, Johnson D, Bodapati A, Keblinski P and Zschack P 2007 *Science* **315** 351–3
[44] Mavrokefalos A, Nguyen N T, Pettes M T, Johnson D C and Shi L 2007 *Appl. Phys. Lett.* **91** 171912
[45] Luckyanova M N, Johnson J A, Maznev A A, Garg J, Jandl A, Bulsara M T, Fitzgerald E A, Nelson K A and Chen G 2013 *Nano Lett.* **13** 3973–7
[46] Luo Z, Maassen J, Deng Y, Du Y, Garrelts R P, Lundstrom M S, Ye P D and Xu X 2015 *Nat. Commun.* **6** 8572
[47] Renteria J D, Ramirez S, Malekpour H, Alonso B, Centeno A, Zurutuza A, Cocemasov A I, Nika D L and Balandin A A 2015 *Adv. Funct. Mater.* **25** 4664–72
[48] Chen J, Chen S and Gao Y 2016 *J. Phys. Chem. Lett.* **7** 2518–23
[49] Chen J, Chen S and Gao Y 2017 *Phys. Rev.* B **95** 134301
[50] Gao Y, Liu Q and Xu B 2016 *ACS Nano* **10** 5431–9
[51] Kang J S, Ke M and Hu Y 2017 *Nano Lett.* **17** 1431–8
[52] Berland K, Arter C A, Cooper V R, Lee K, Lundqvist B I, Schröder E, Thonhauser T and Hyldgaard P 2014 *J. Chem. Phys.* **140** 18A539
[53] Broido D A, Malorny M, Birner G, Mingo N and Stewart D A 2007 *Appl. Phys. Lett.* **91** 231922
[54] Ward A, Broido D A, Stewart D A and Deinzer G 2009 *Phys. Rev.* B **80** 125203
[55] Ward A and Broido D A 2010 *Phys. Rev.* B **81** 085205
[56] Fugallo G, Lazzeri M, Paulatto L and Mauri F 2013 *Phys. Rev.* B **88** 045430
[57] Garg J, Bonini N, Kozinsky B and Marzari N 2011 *Phys. Rev. Lett.* **106** 045901
[58] Lindsay L, Broido D A and Reinecke T L 2012 *Phys. Rev. Lett.* **109** 095901
[59] Lindsay L, Broido D A and Reinecke T L 2013 *Phys. Rev. Lett.* **111** 025901
[60] Bonini N, Garg J and Marzari N 2012 *Nano Lett.* **12** 2673–8
[61] Fugallo G, Cepellotti A, Paulatto L, Lazzeri M, Marzari N and Mauri F 2014 *Nano Lett.* **14** 6109–14
[62] Zeraati M, Vaez Allaei S M, Abdolhosseini Sarsari I, Pourfath M and Donadio D 2016 *Phys. Rev.* B **93** 085424
[63] Tamura S I 1983 *Phys. Rev.* B **27** 858–66
[64] Berglund M and Wieser M E 2011 *Pure Appl. Chem.* **83** 397–410
[65] Petkov V, Billinge S J L, Larson P, Mahanti S D, Vogt T, Rangan K K and Kanatzidis M G 2002 *Phys. Rev.* B **65** 092105
[66] Mulhern P J 1989 *Can. J. Phys.* **67** 1049–52
[67] Jiang P, Qian X, Gu X and Yang R 2017 *Adv. Mater.* **29** 1701068
[68] Cheng Y, Nie A, Zhang Q, Gan L Y, Shahbazian-Yassar R and Schwingenschlögl U 2014 *ACS Nano* **8** 11447–53
[69] Somoano R B, Hadek V and Rembaum A 1973 *J. Chem. Phys.* **58** 697–701
[70] Py M A and Haering R R 1983 *Can. J. Phys.* **61** 76–84
[71] Rocquefelte X, Bouessay I, Boucher F, Gressier P and Ouvrard G 2003 *J. Solid State Chem.* **175** 380–3
[72] Jahn H A and Teller E 1937 *Proc. R. Soc.* A **161** 220–35
[73] Sood A, Xiong F, Chen S, Cheaito R, Lian F, Asheghi M, Cui Y, Donadio D, Goodson K E and Pop E 2019 *Nano Lett.* (https://doi.org/10.1021/acs.nanolett.8b05174)
[74] Meng X *et al* 2017 (arXiv:1708.03849 [cond-mat])
[75] Greaves G N, Greer A L, Lakes R S and Rouxel T 2011 *Nat. Mater.* **10** 823–37
[76] Jiang J W and Park H S 2014 *Nat. Commun.* **5** 4727
[77] Woo S, Park H C and Son Y W 2016 *Phys. Rev.* B **93** 075420
[78] Ding Z, Pei Q X, Jiang J W and Zhang Y W 2015 *J. Phys. Chem.* C **119** 16358–65
[79] Sparavigna A 2002 *Phys. Rev.* B **66** 174301
[80] Li W, Lindsay L, Broido D A, Stewart D A and Mingo N 2012 *Phys. Rev.* B **86** 174307
[81] Li W, Carrete J, Katcho N A and Mingo N 2014 *Comput. Phys. Commun.* **185** 1747–58
[82] Perdew J P and Zunger A 1981 *Phys. Rev.* B **23** 5048–79
[83] Giannozzi P *et al* 2009 *J. Phys.: Condens. Matter* **21** 395502
[84] Giannozzi P *et al* 2017 *J. Phys.: Condens. Matter* **29** 465901
[85] Hartwigsen C, Goedecker S and Hutter J 1998 *Phys. Rev.* B **58** 3641–62
[86] Baroni S, de Gironcoli S, Dal Corso A and Giannozzi P 2001 *Rev. Mod. Phys.* **73** 515–62
[87] Thonhauser T, Zuluaga S, Arter C, Berland K, Schröder E and Hyldgaard P 2015 *Phys. Rev. Lett.* **115** 136402
[88] Thonhauser T, Cooper V R, Li S, Puzder A, Hyldgaard P and Langreth D C 2007 *Phys. Rev.* B **76** 125112
[89] Berland K, Cooper V R, Lee K, Schröder E, Thonhauser T, Hyldgaard P and Lundqvist B I 2015 *Rep. Prog. Phys.* **78** 066501
[90] Langreth D C *et al* 2009 *J. Phys.: Condens. Matter* **21** 084203
[91] Berland K and Hyldgaard P 2014 *Phys. Rev.* B **89** 035412
[92] Blöchl P E 1994 *Phys. Rev.* B **50** 17953–79
[93] Kresse G and Joubert D 1999 *Phys. Rev.* B **59** 1758–75
[94] Wakabayashi N, Smith H G and Nicklow R M 1975 *Phys. Rev.* B **12** 659–63
[95] Tornatzky H, Gillen R, Uchiyama H and Maultzsch J 2018 (arXiv:1809.03381)

Supplementary Information:

Strongly tunable anisotropic thermal transport in MoS_2 by strain and Li intercalation: First principles calculations

Shunda Chen[1,*], Aditya Sood[2,3,6], Eric Pop[2,4,5], Kenneth E. Goodson[3], Davide Donadio[1,*]

[1]*Department of Chemistry, University of California, Davis, CA 95616, USA.*

[2]*Department of Electrical Engineering, Stanford University, Stanford, CA 94305, USA.*

[3]*Department of Mechanical Engineering, Stanford University, Stanford, CA 94305, USA.*

[4]*Department of Materials Science and Engineering, Stanford University, Stanford, CA 94305, USA.* [5]*Precourt Institute for Energy, Stanford University, Stanford, CA 94305, USA.* [6]*Present address: Stanford Institute for Materials and Energy Sciences, SLAC National Accelerator Laboratory, Menlo Park, CA 94025, USA*

[*] Email: shdchen@ucdavis.edu, ddonadio@ucdavis.edu

List of Supplementary Figures:

Figure S15. Full phonon dispersion curves for $LiMoS_2$ under different strains.

Figure S16. Cross-plane thermal conductivity of MoS_2 from the self-consistent (**SCF**) solution and relaxation time approximation (**RTA**) of the Boltzmann transport equation, as a function of the size of the q-point grid at T = 300 K. (11th nearest neighbor.)

Figure S17. In-plane thermal conductivity of MoS_2 from the self-consistent (**SCF**) solution and relaxation time approximation (**RTA**) of the Boltzmann transport equation, as a function of the size of the q-point grid at T = 300 K. (11th nearest neighbor.)

Figure S18. Cross-plane thermal conductivity of $LiMoS_2$ from the self-consistent (**SCF**) solution and relaxation time approximation (**RTA**) of the Boltzmann transport equation, as a function of the size of the q-point grid at T = 300 K.

Figure S19. In-plane thermal conductivity of $LiMoS_2$ from the self-consistent (**SCF**) solution and relaxation time approximation (**RTA**) of the Boltzmann transport equation, as a function of the size of the q-point grid at T = 300 K.

Figure S20. Phonon dispersion relations for MoS_2 by LDA and vdW-DF.

Figure S21. Phonon dispersion relations for MoS_2 with vdW-DF, compared with experimental data (black circles, neutron scattering data on bulk MoS_2 crystals. [Wakabayashi, N.; Smith, H. G.; Nicklow, R. M. *Phys. Rev. B* **1975**, *12* (2), 659–663])

Figure S22. Cross-plane (a) and in-plane (b) thermal conductivity as a function of strain for MoS_2 with LDA (blue circles) and vdW-DF (red squares).

Figure S23. Anisotropy ratio of in-plane thermal conductivity to cross-plane thermal conductivity VS strain, for MoS_2 with LDA (blue circles) and vdW-DF (red squares).

Figure S24. Phonon dispersion relations for $LiMoS_2$ by LDA compared to those by vdW-DF.

Figure S25. Comparison between thermal conductivities of isotopically pure systems and those of naturally occurring systems under cross-plane strain.

Figure S26. The Poisson's ratio as a function of cross-plane strain for pristine MoS_2 by LDA and vdW-DF.

Figure S27. The Poisson's ratio as a function of cross-plane strain for $LiMoS_2$ by LDA and vdW-DF.

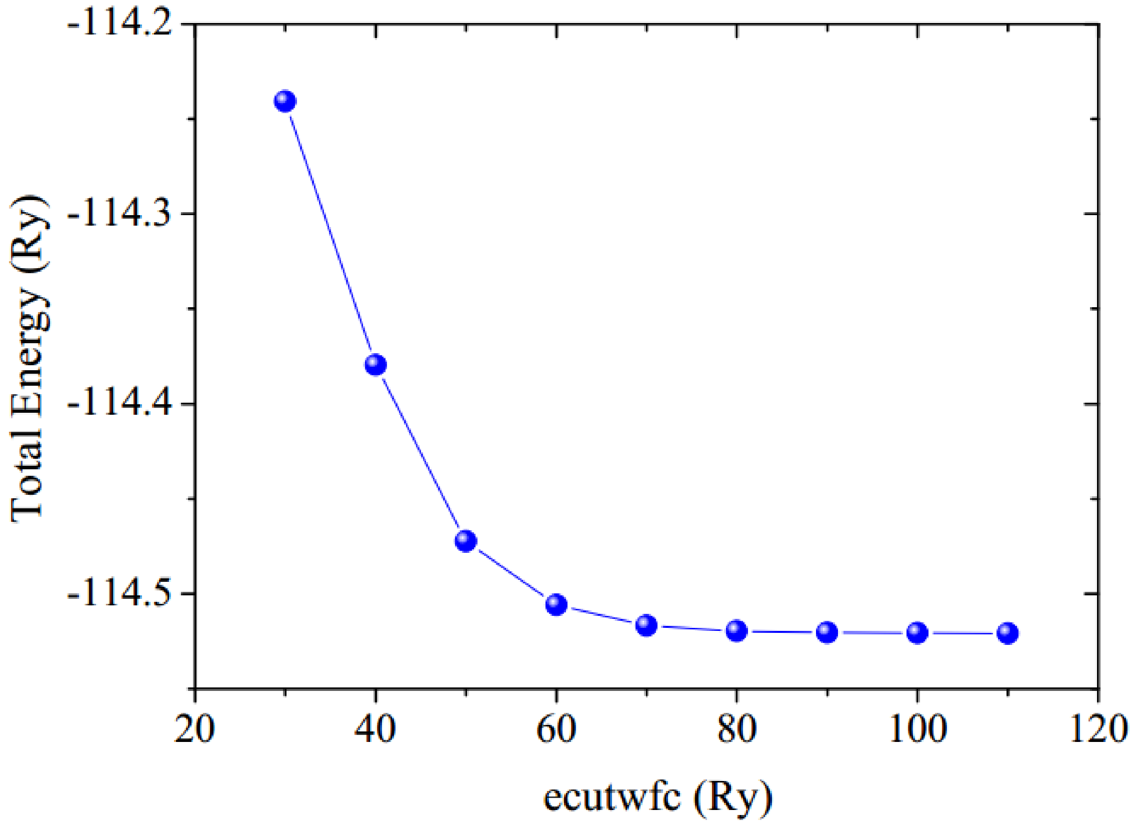

Figure S1. The total energy convergence with plane wave cutoff ecutwfc for MoS_2 with LDA.

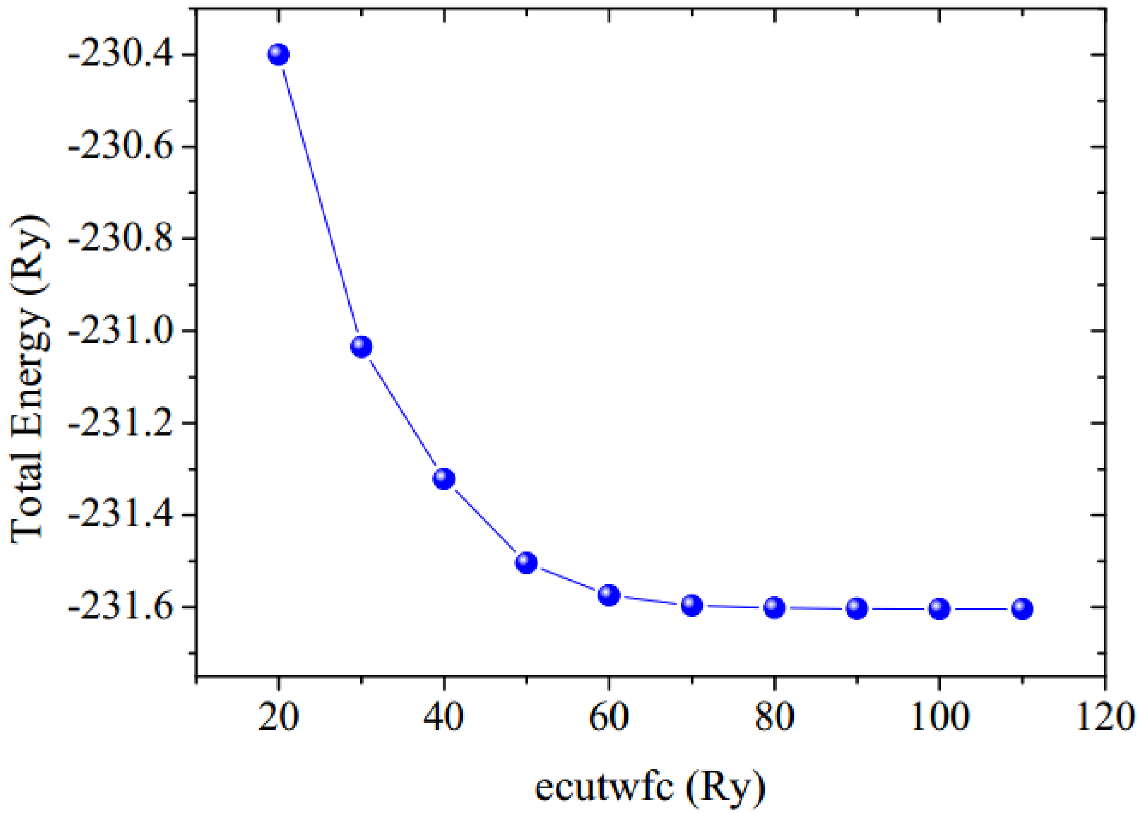

Figure S2. The total energy convergence with plane wave cutoff ecutwfc for $LiMoS_2$ with LDA.

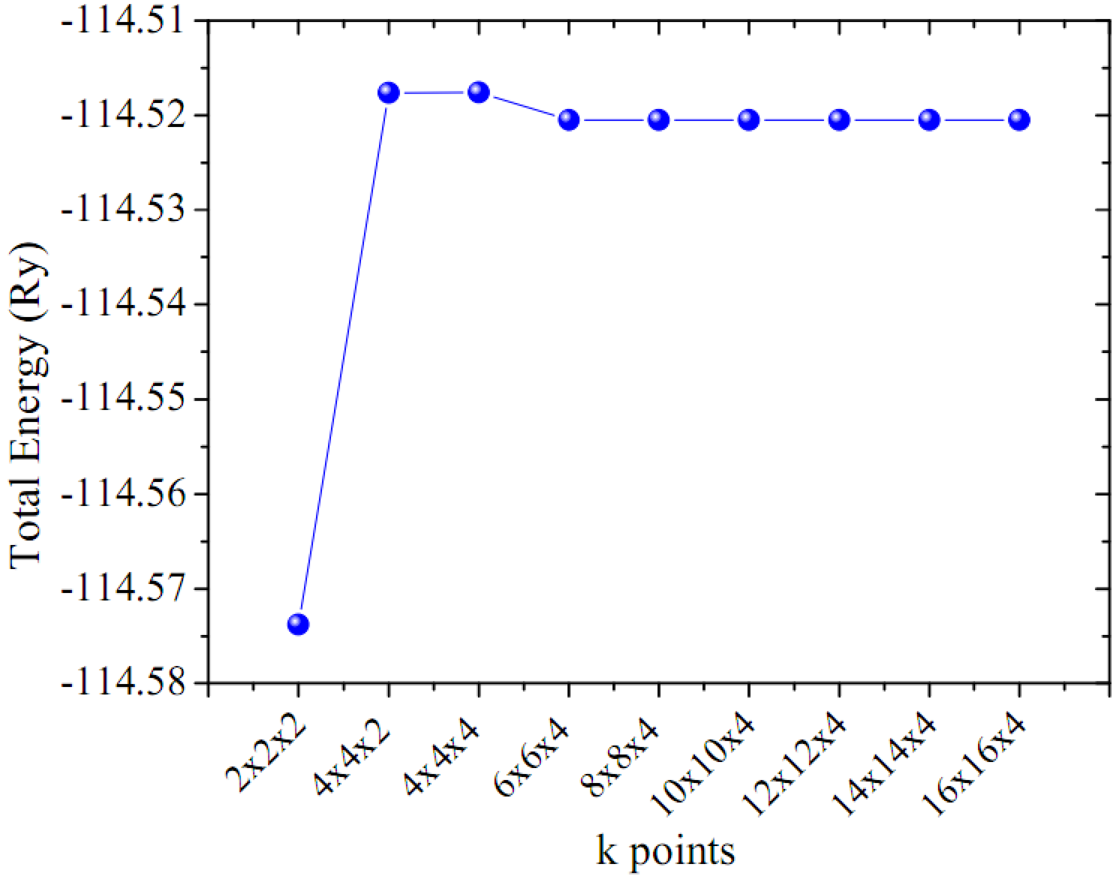

Figure S3. The total energy convergence with k points for MoS_2 with LDA.

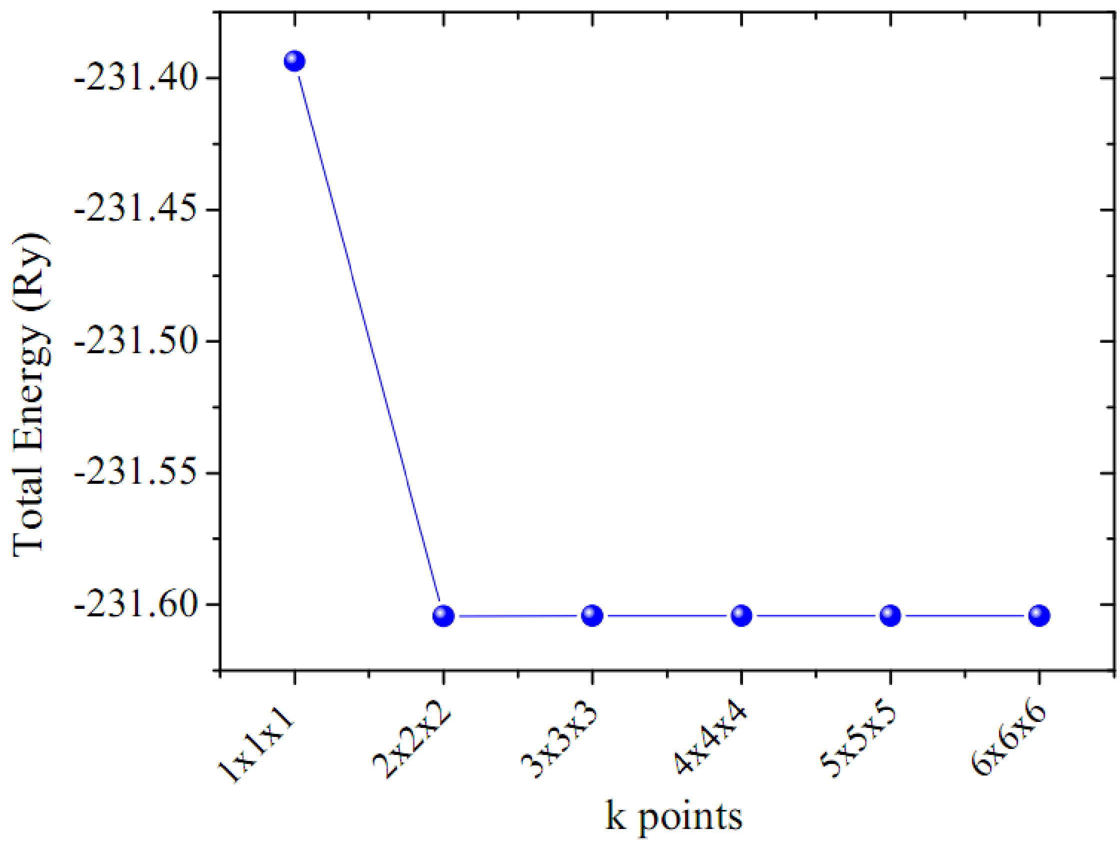

Figure S4. The total energy convergence with k points for $LiMoS_2$ with LDA.

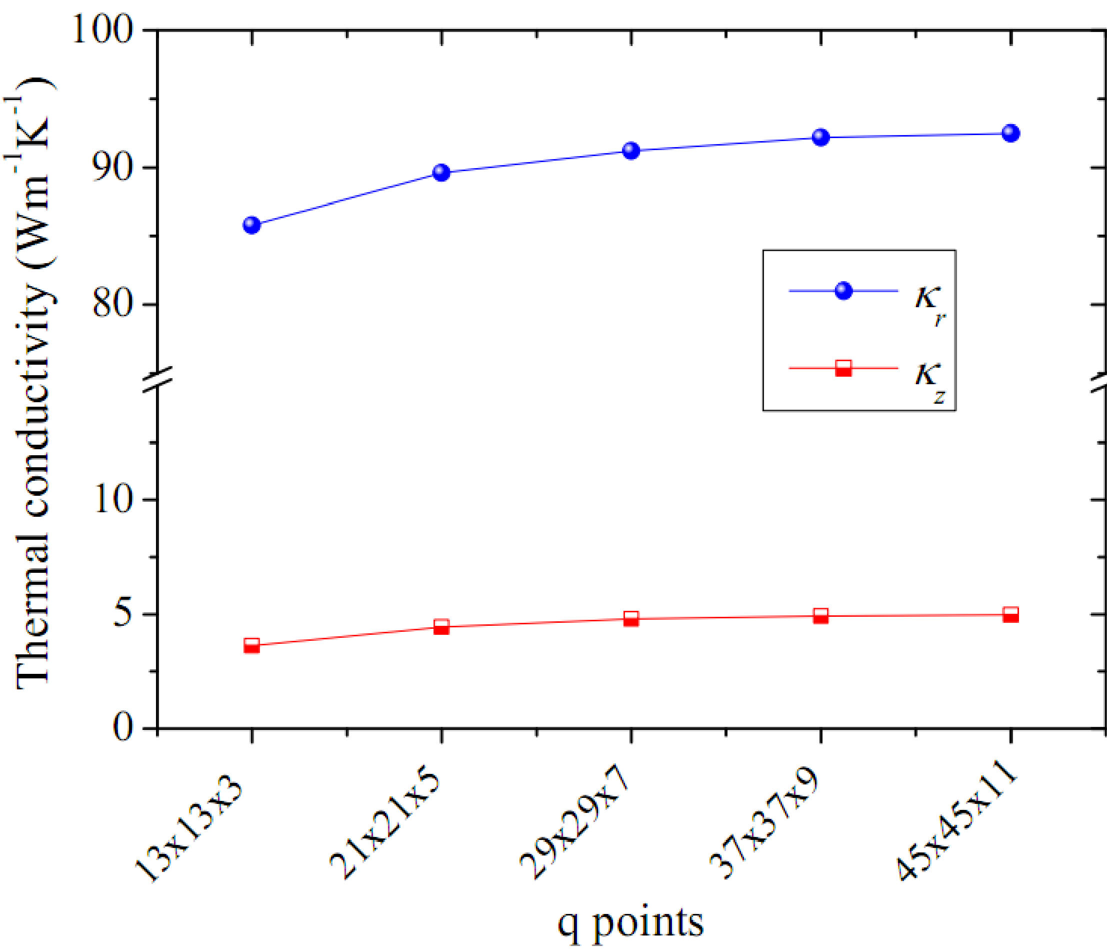

Figure S5. In-plane and cross-plane thermal conductivity of MoS_2 with LDA, from the solution of the Boltzmann transport equation, as a function of the size of the q-point grid used to represent phonons in the first Brillouin zone at T = 300 K.

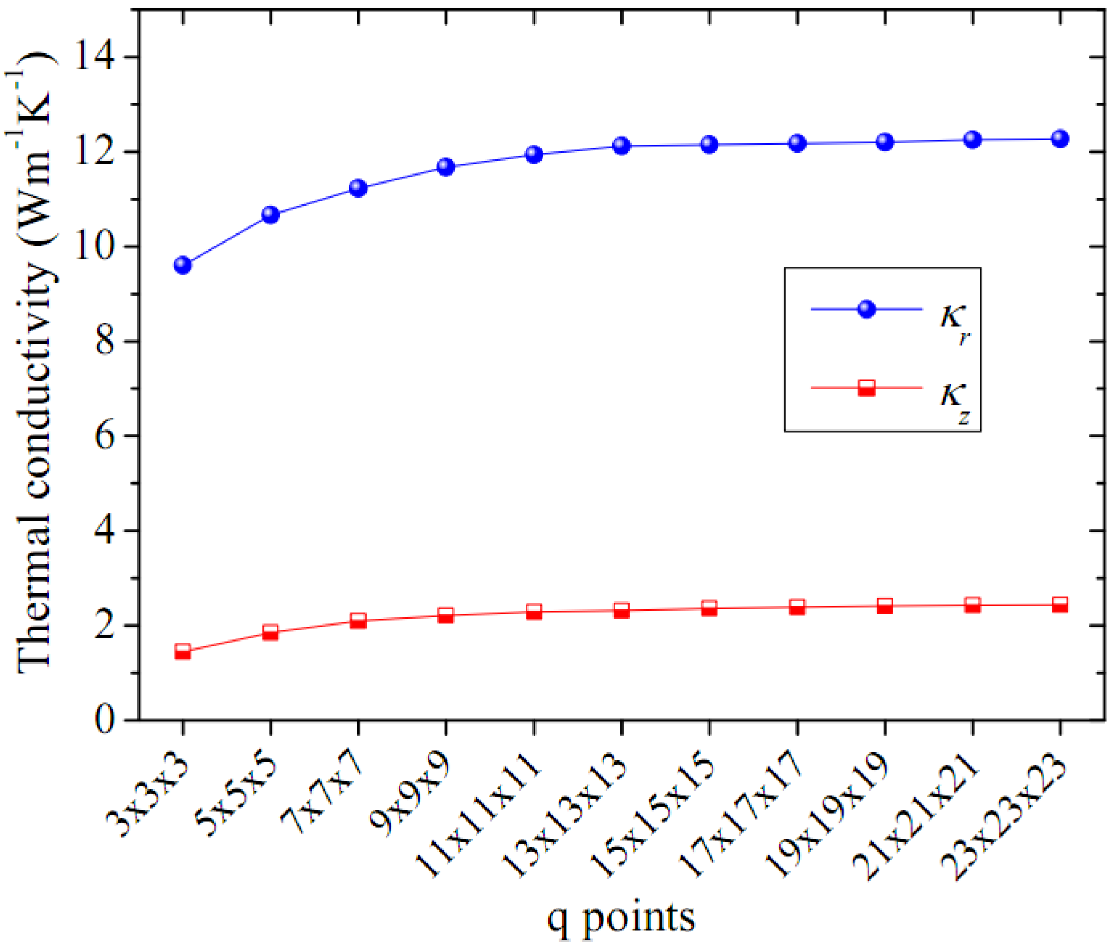

Figure S6. In-plane and cross-plane thermal conductivity of $LiMoS_2$ with LDA, from the solution of the Boltzmann transport equation, as a function of the size of the q-point grid used to represent phonons in the first Brillouin zone at T = 300 K.

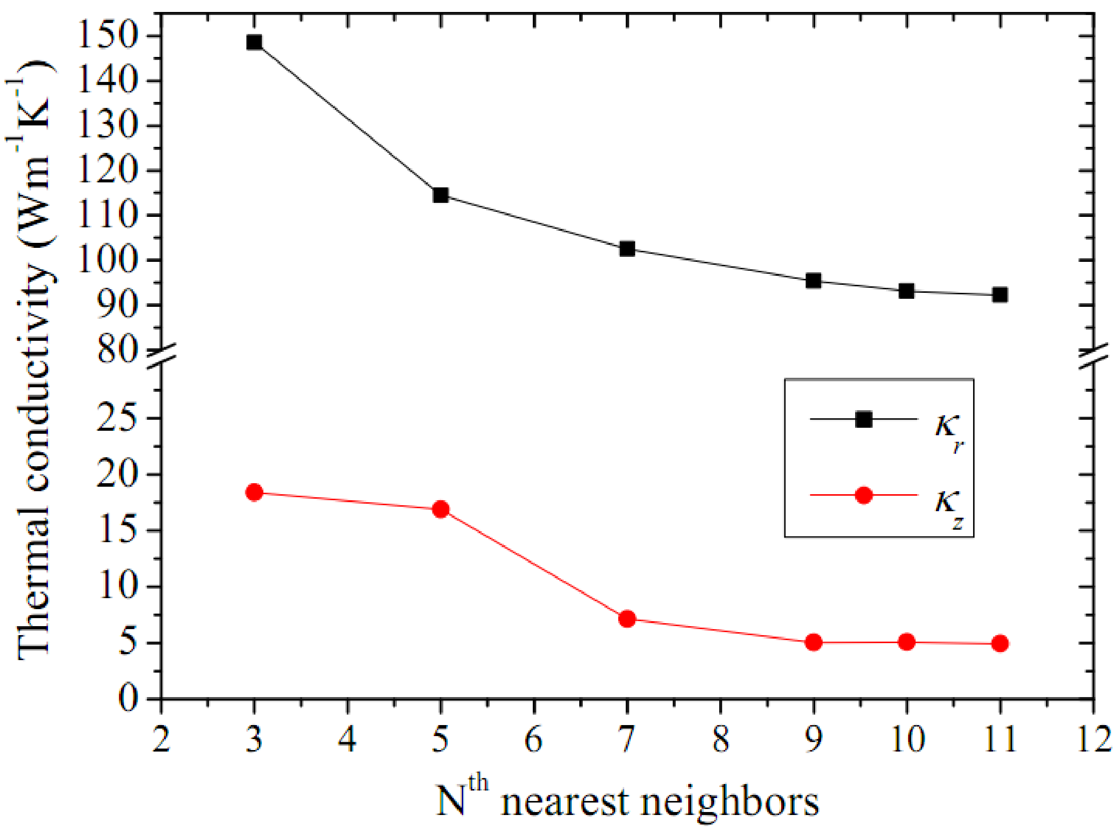

Figure S7. In-plane and cross-plane thermal conductivity of MoS_2 with LDA, as a function of the interactions up to N^{th} nearest neighbors for the anharmonic force constants at T = 300 K.

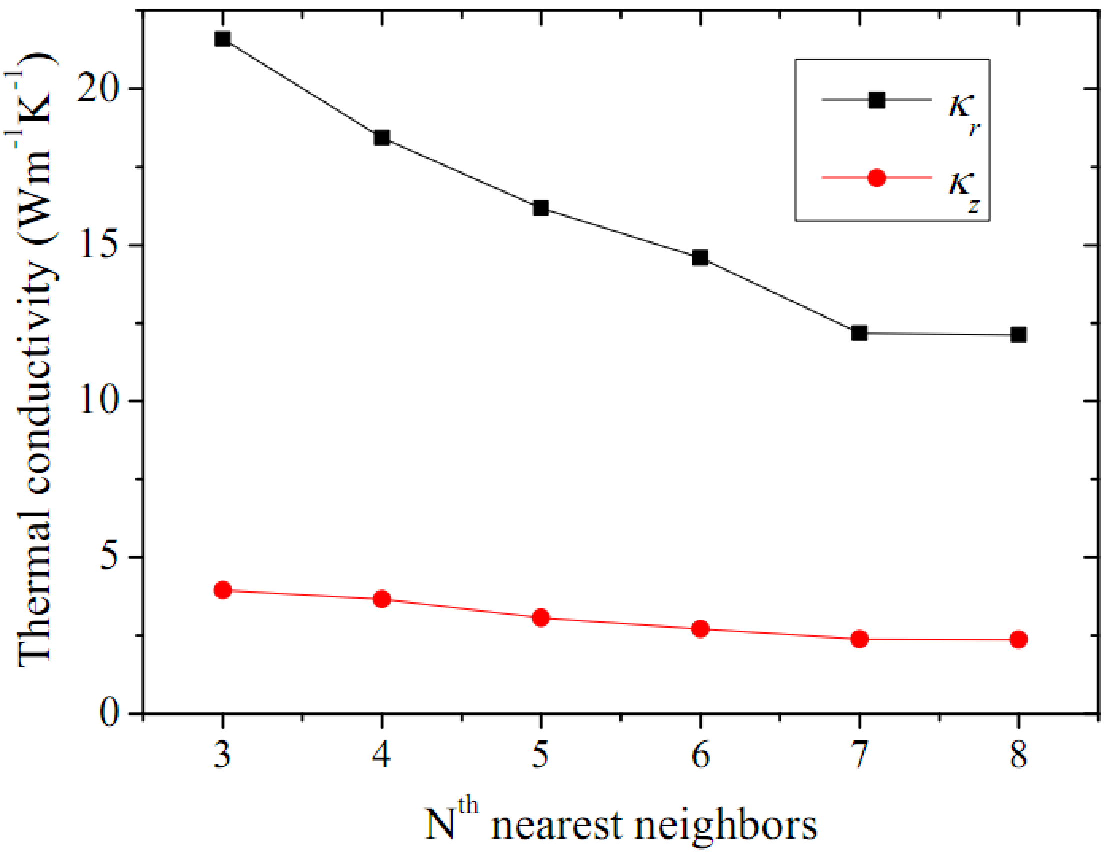

Figure S8. In-plane and cross-plane thermal conductivity of $LiMoS_2$ with LDA, as a function of the interactions up to Nth nearest neighbors for the anharmonic force constants at T = 300 K.

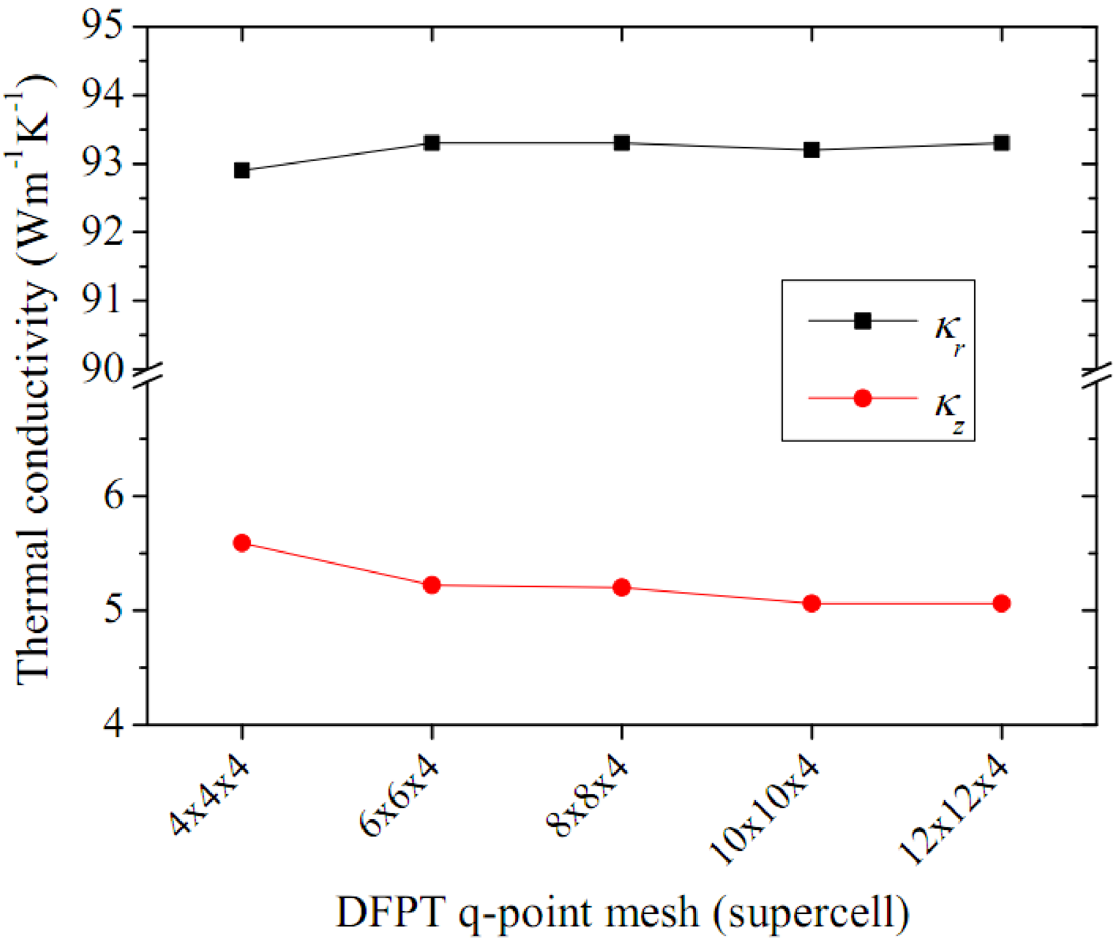

Figure S9. Convergence of in-plane and cross-plane thermal conductivity of MoS2 (with LDA), as a function of the DFPT q-point mesh (supercell size) for the calculation of the harmonic force constants (T=300 K).

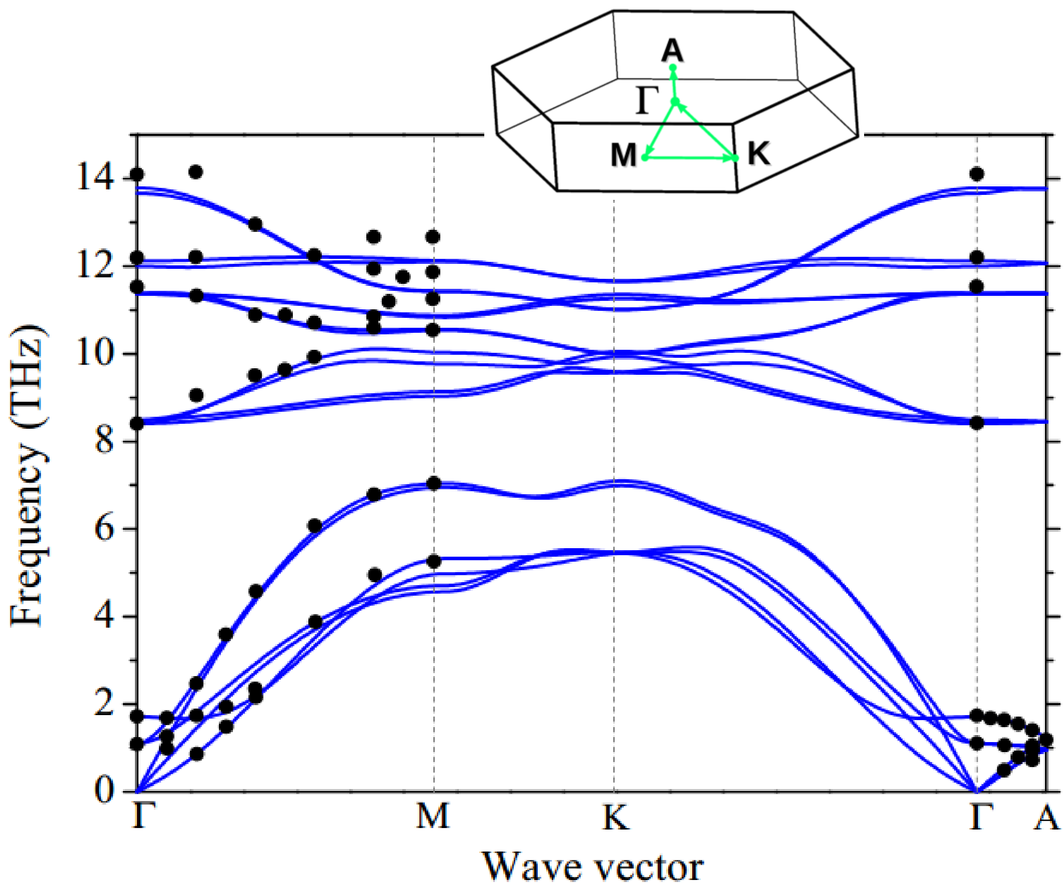

Figure S10. Phonon dispersion relations for MoS_2 with LDA, compared with experimental data (black circles, neutron scattering data on bulk MoS_2 crystals, [Wakabayashi, N.; Smith, H. G.; Nicklow, R. M. *Phys. Rev. B* **1975**, *12* (2), 659–663])

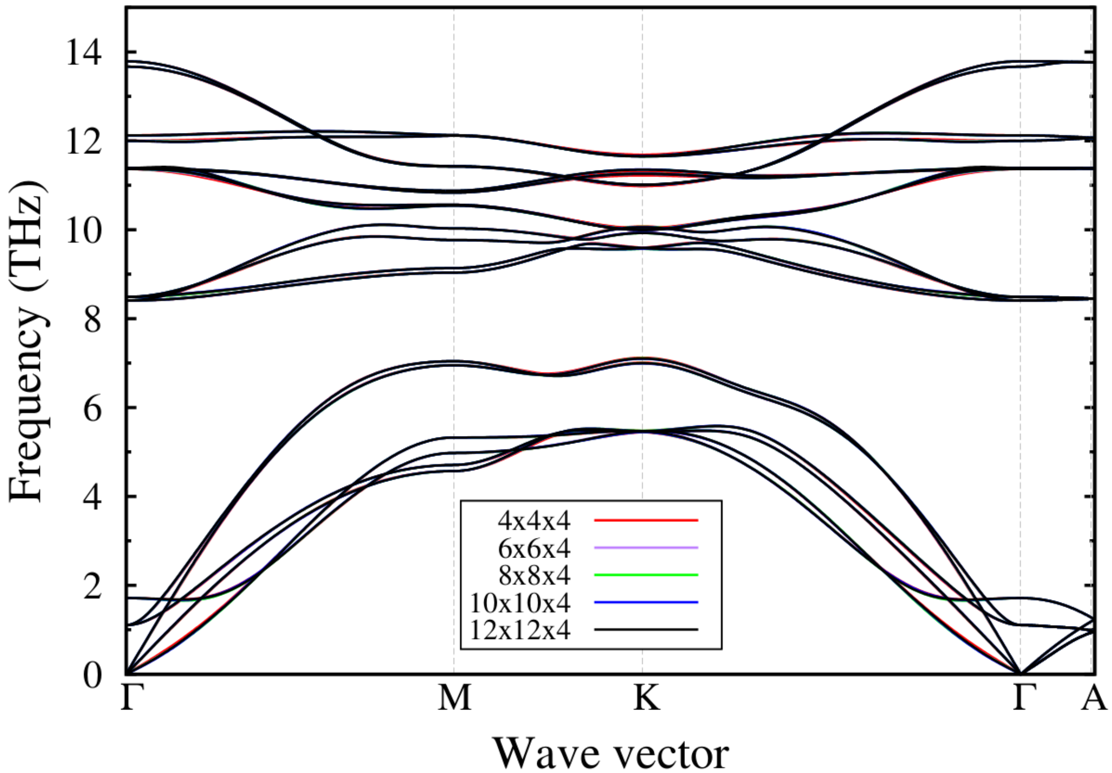

Figure S11. Phonon dispersion relations as a function of the DFPT q-point mesh (supercell size) for MoS_2.

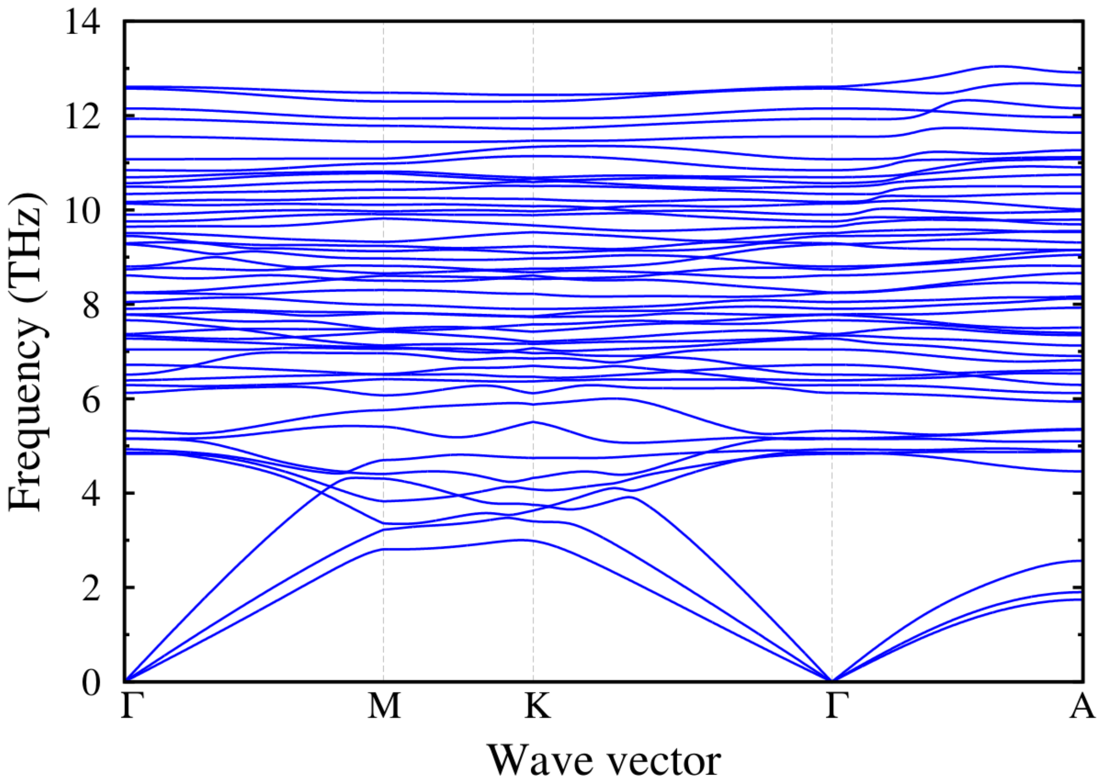

Figure S12. Phonon dispersion relations for $LiMoS_2$ by DFPT with q-point mesh 4x4x4.

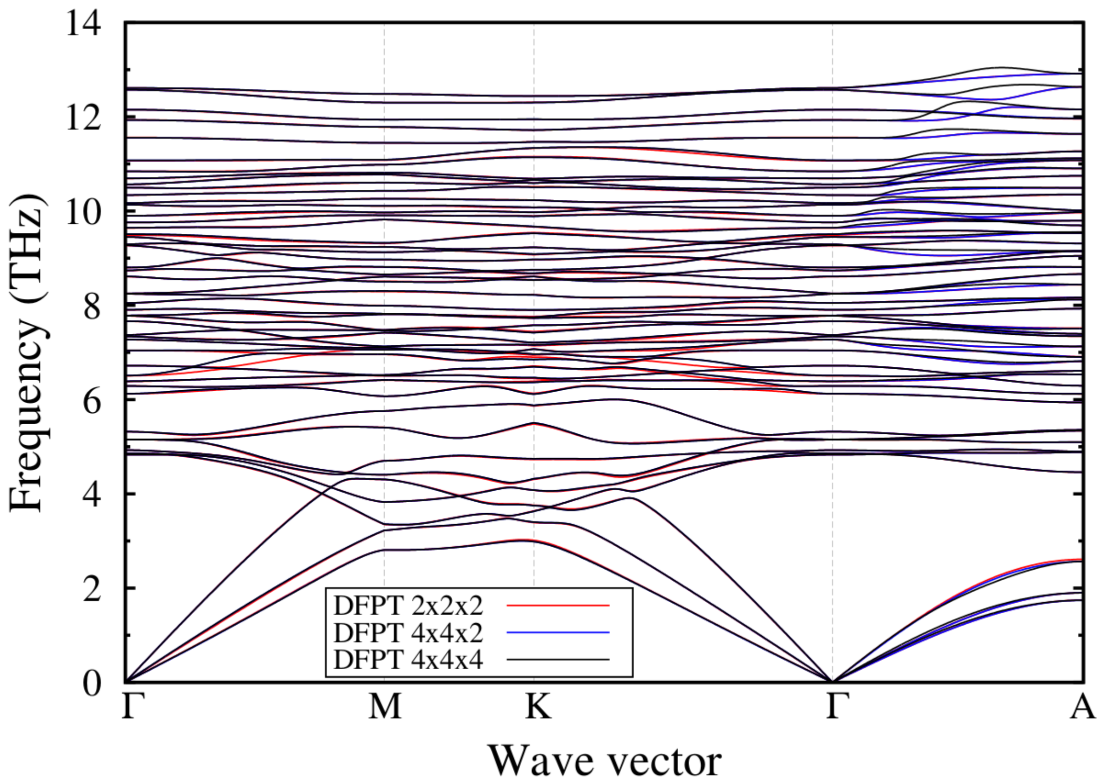

Figure S13. Phonon dispersion relations of $LiMoS_2$ as a function of the DFPT q-point mesh (supercell size).

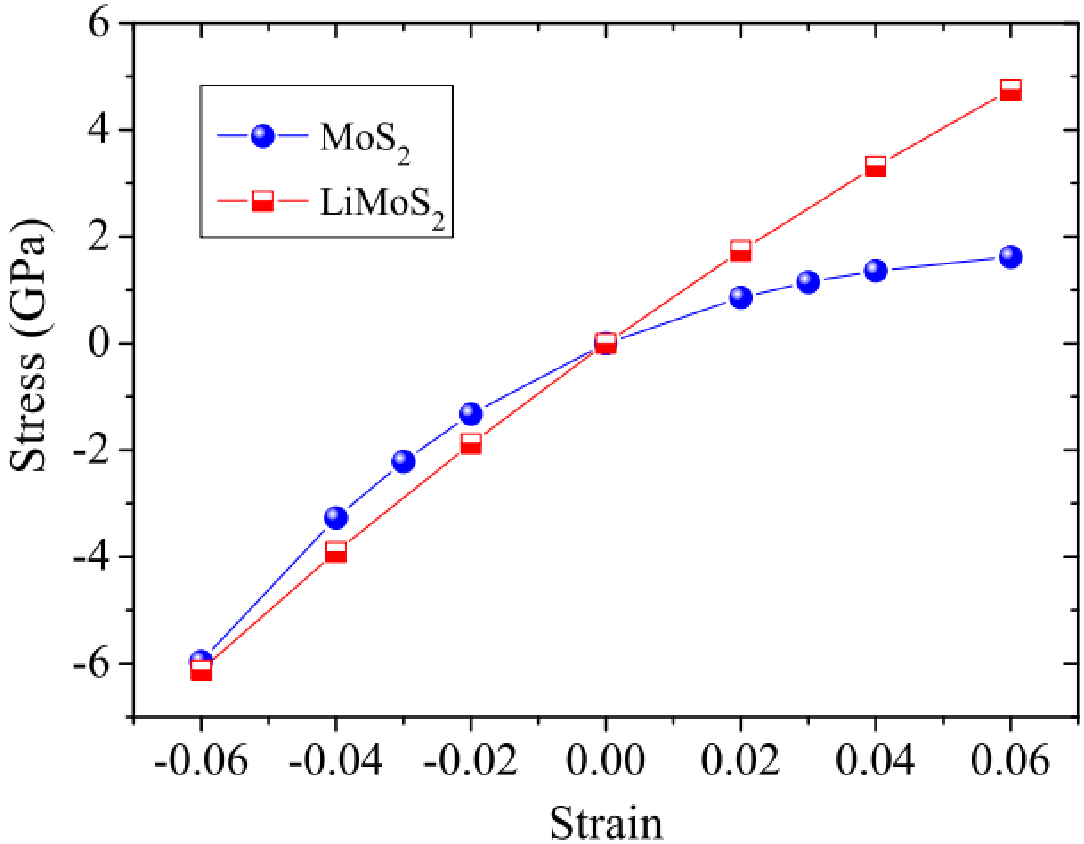

Figure S14. Stress-strain curves for pristine MoS_2 and $LiMoS_2$.

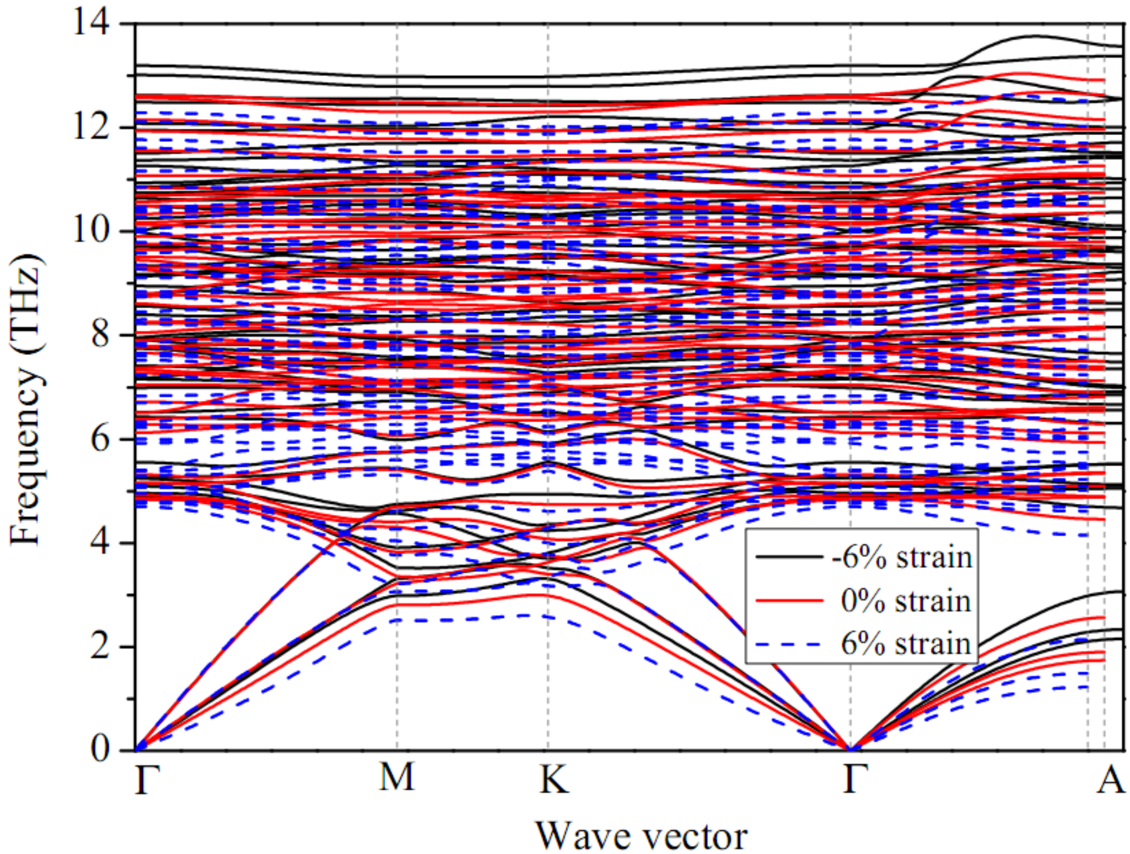

Figure S15. Full phonon dispersion curves for $LiMoS_2$ under different strains.

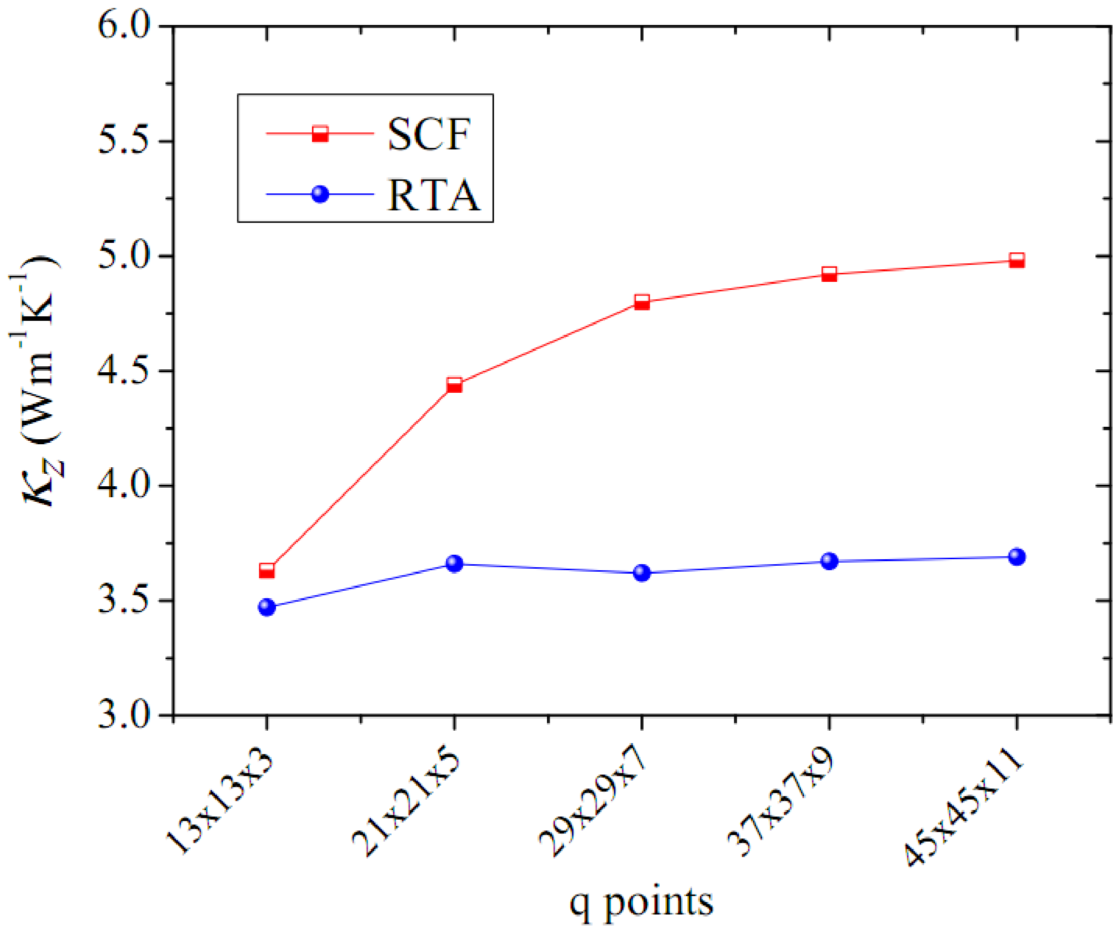

Figure S16. Cross-plane thermal conductivity of MoS_2 from the self-consistent (**SCF**) solution and relaxation time approximation (**RTA**) of the Boltzmann transport equation, as a function of the size of the q-point grid at T = 300 K. (11th nearest neighbor.)

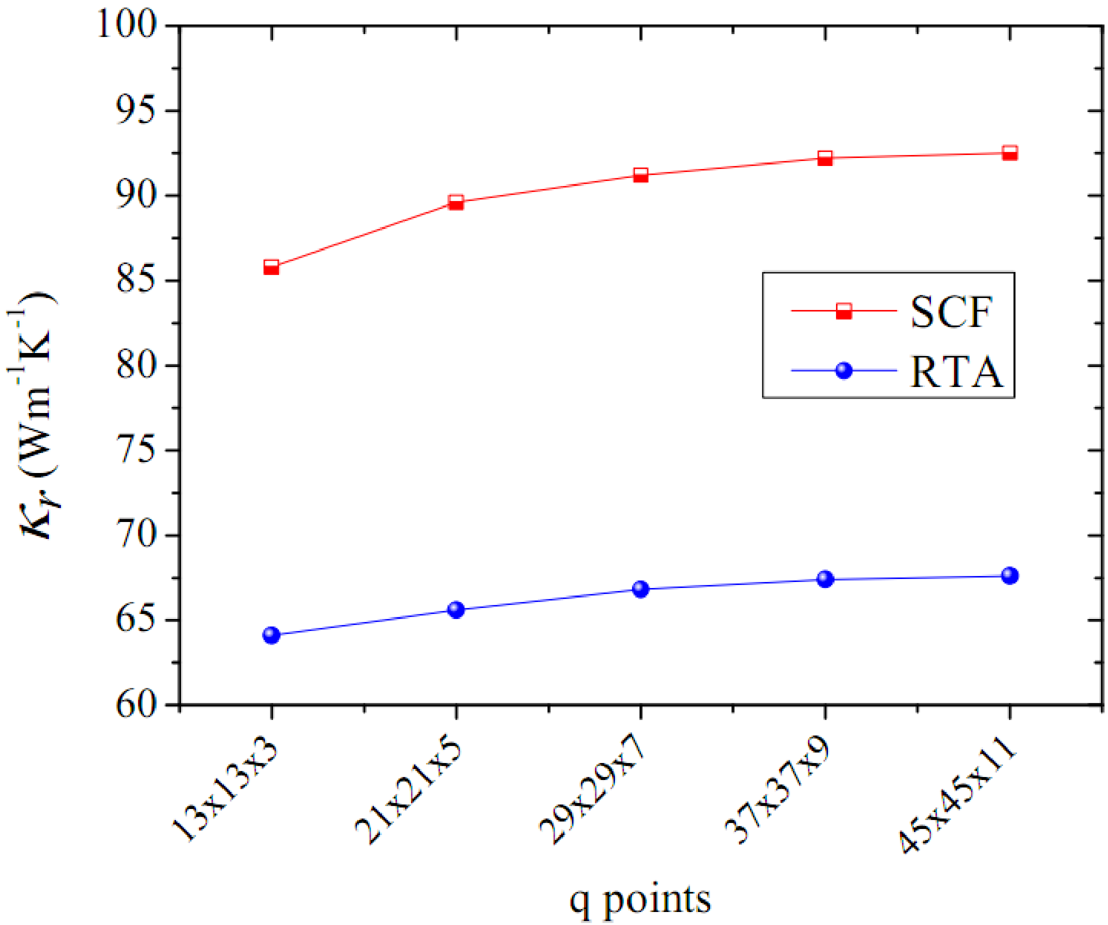

Figure S17. In-plane thermal conductivity of MoS_2 from the self-consistent (**SCF**) solution and relaxation time approximation (**RTA**) of the Boltzmann transport equation, as a function of the size of the q-point grid at T = 300 K. (11^{th} nearest neighbor.)

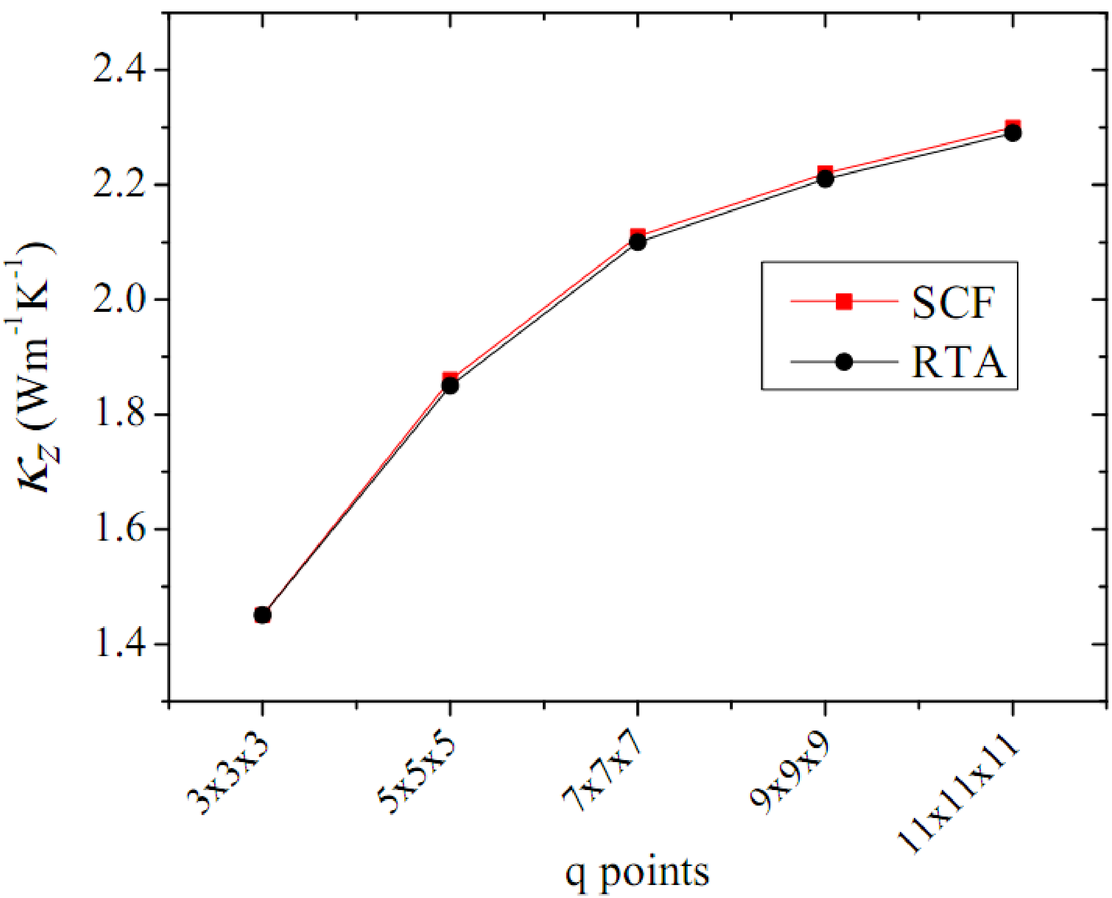

Figure S18. Cross-plane thermal conductivity of $LiMoS_2$ from the self-consistent (**SCF**) solution and relaxation time approximation (**RTA**) of the Boltzmann transport equation, as a function of the size of the q-point grid at T = 300 K.

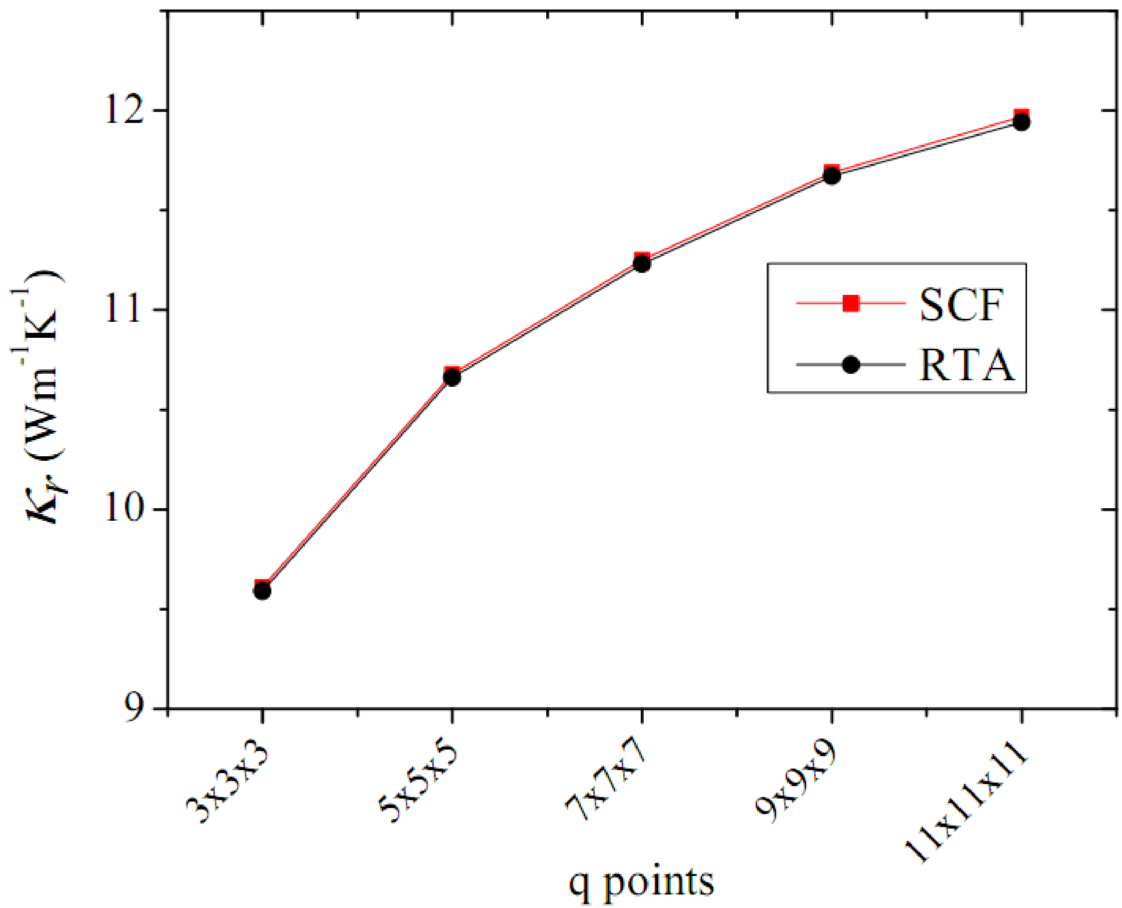

Figure S19. In-plane thermal conductivity of $LiMoS_2$ from the self-consistent (**SCF**) solution and relaxation time approximation (**RTA**) of the Boltzmann transport equation, as a function of the size of the q-point grid at T = 300 K.

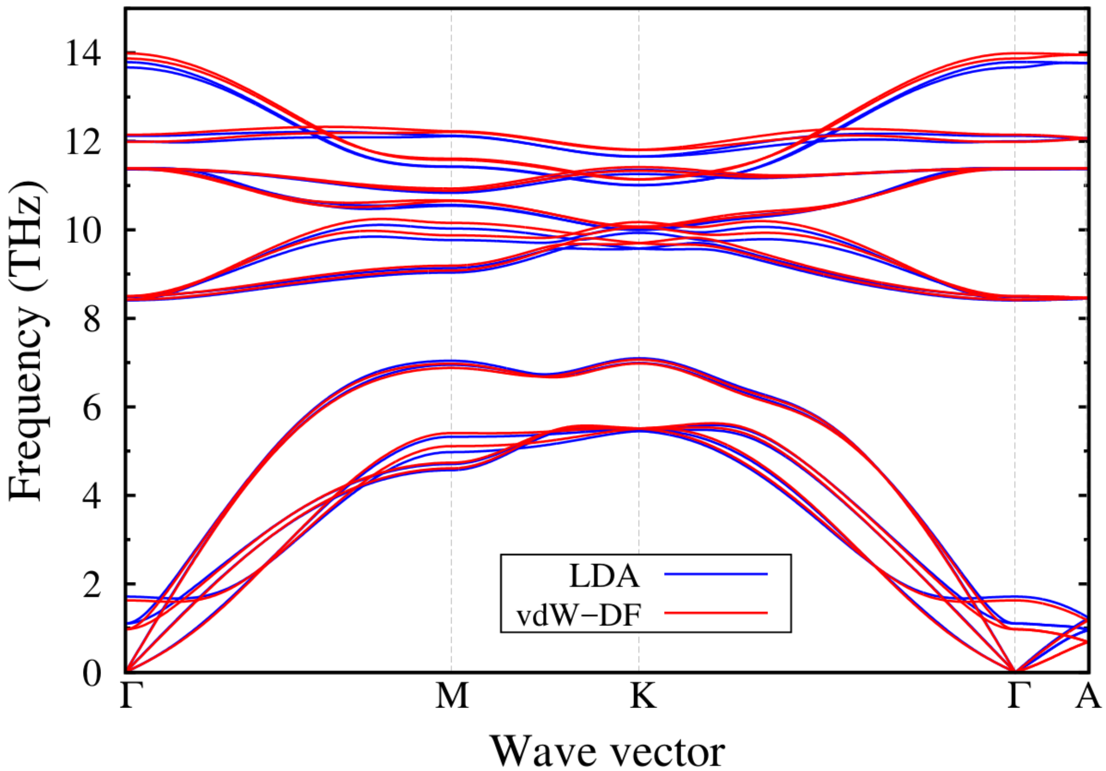

Figure S20. Phonon dispersion relations for MoS_2 by LDA (blue lines) and vdW-DF (red lines).

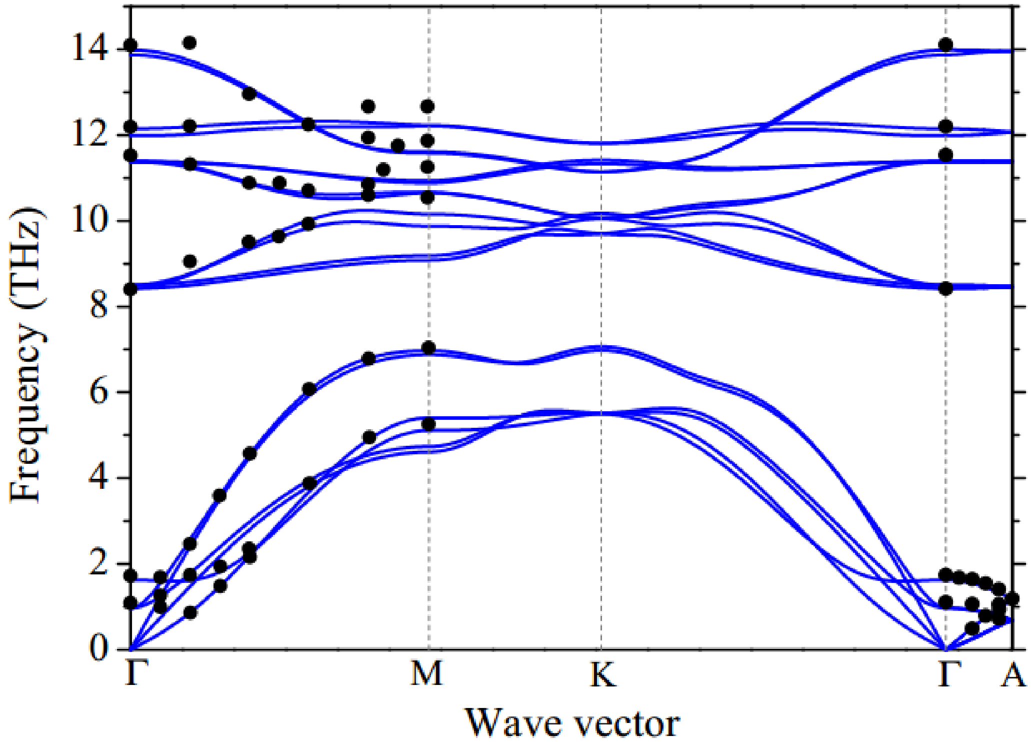

Figure S21. Phonon dispersion relations for MoS_2 with vdW-DF, compared with experimental data (black circles, neutron scattering data on bulk MoS_2 crystals. [Wakabayashi, N.; Smith, H. G.; Nicklow, R. M. *Phys. Rev. B* **1975**, *12* (2), 659–663])

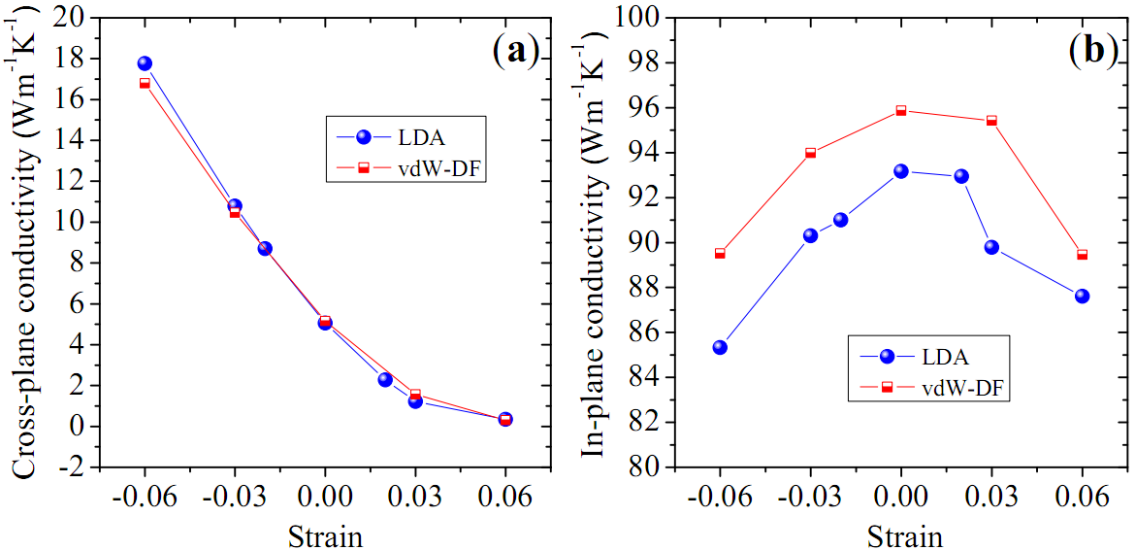

Figure S22. Cross-plane (a) and in-plane (b) thermal conductivity as a function of strain for MoS_2 with LDA (blue circles) and vdW-DF (red squares).

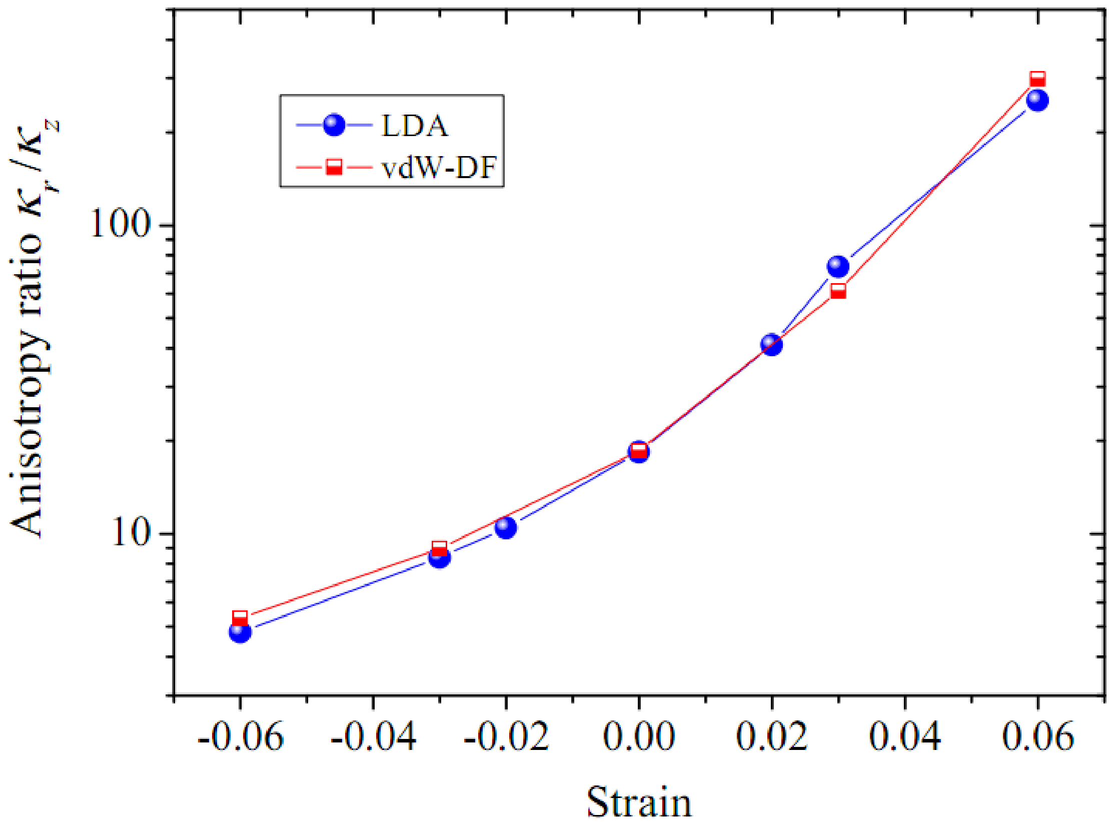

Figure S23. Anisotropy ratio of in-plane thermal conductivity to cross-plane thermal conductivity VS strain, for MoS_2 with LDA (blue circles) and vdW-DF (red squares).

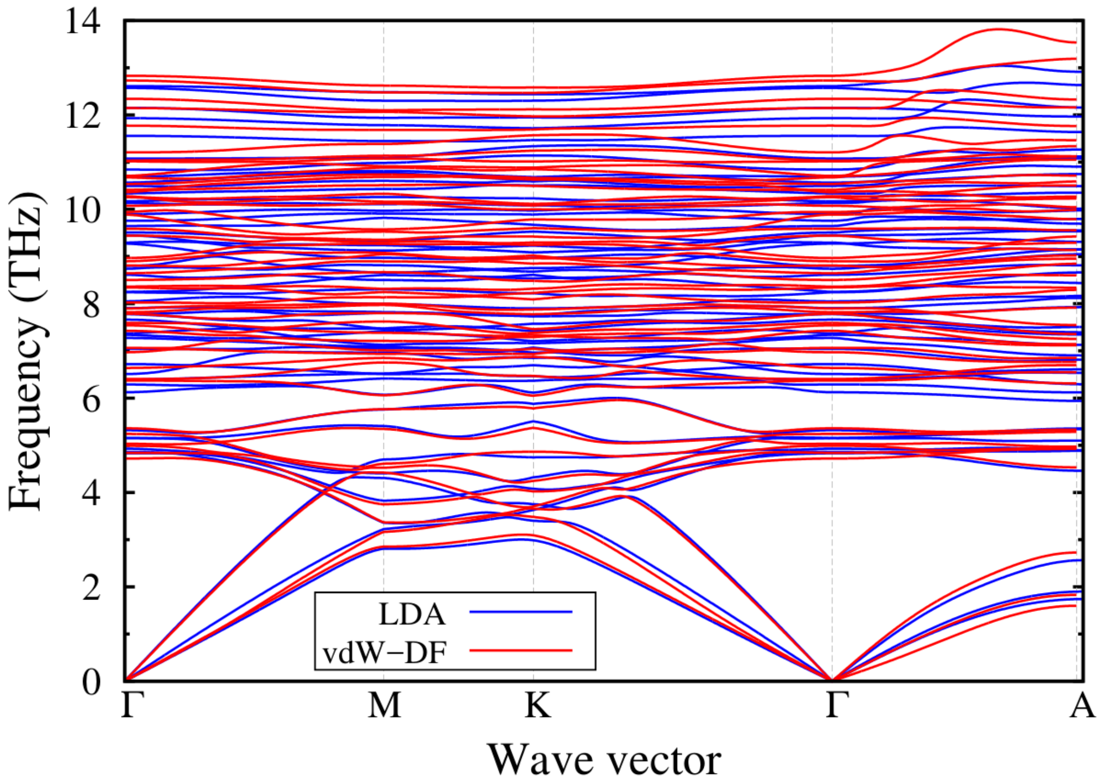

Figure S24. Phonon dispersion relations for $LiMoS_2$ by LDA (blue lines) compared to those by vdW-DF (red lines).

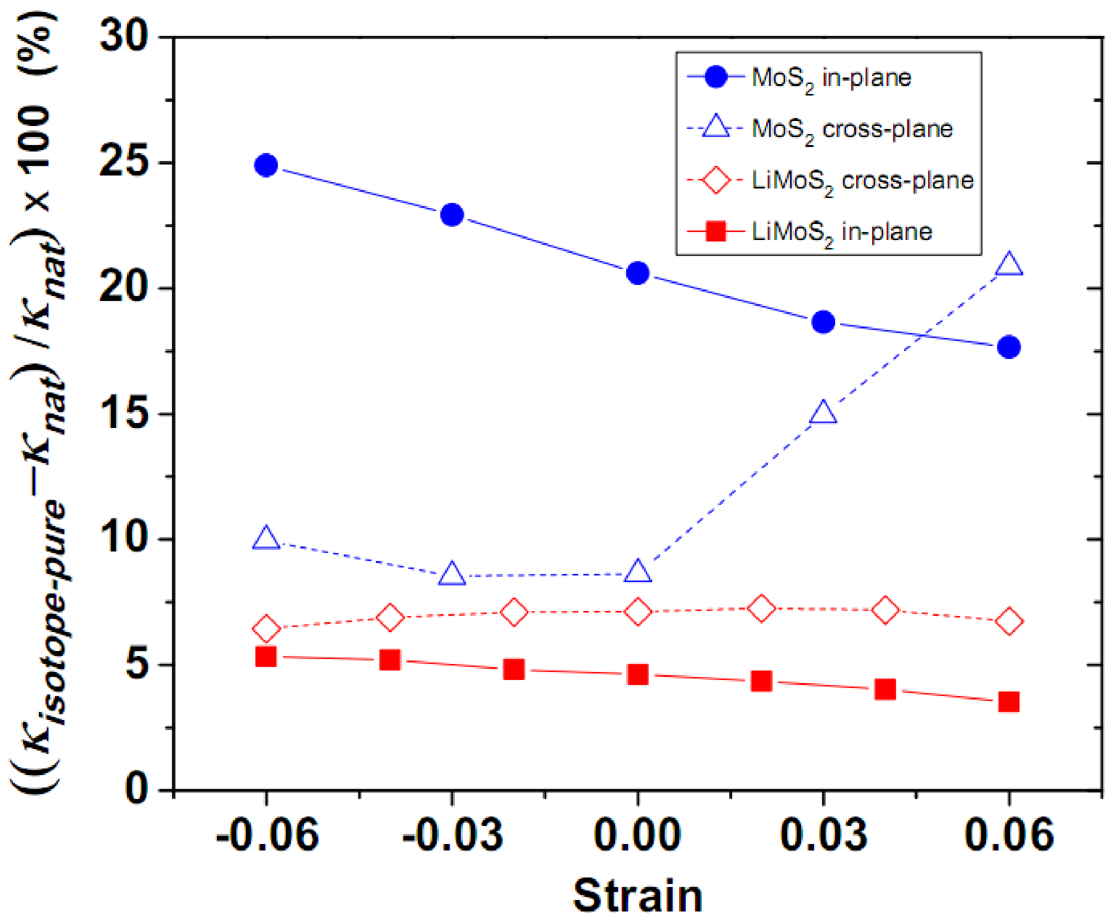

Figure S25. Comparison between thermal conductivities of isotopically pure systems ($\kappa_{isotope-pure}$) and those of natural isotopic compositions (κ_{nat}) under cross-plane strain.

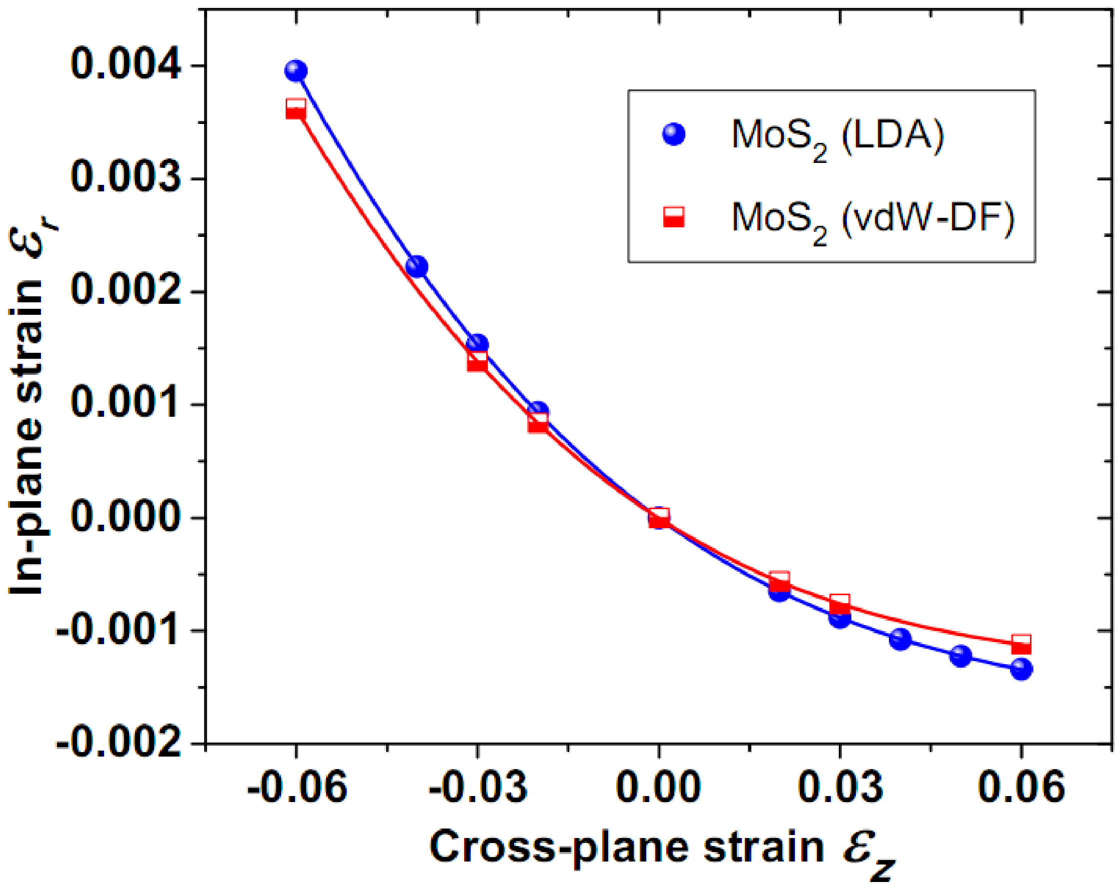

Figure S26. The Poisson's ratio as a function of cross-plane strain for MoS_2 by LDA (blue circles) and vdW-DF (red squares). In-plane strain ε_r versus cross-plane strain ε_z. Data are fitted to function $y = -\nu_1 x + \nu_2 x^2 + \nu_3 x^3$, with $\nu_1 = 0.0389$ (as the linear Poisson's ratio), $\nu_2 = 0.362$ and $\nu_3 = -1.455$ for pristine MoS_2 with LDA (blue line); $\nu_1 = 0.0345$ (as the linear Poisson's ratio), $\nu_2 = 0.347$ and $\nu_3 = -1.406$ for pristine MoS_2 with vdW-DF (red line).

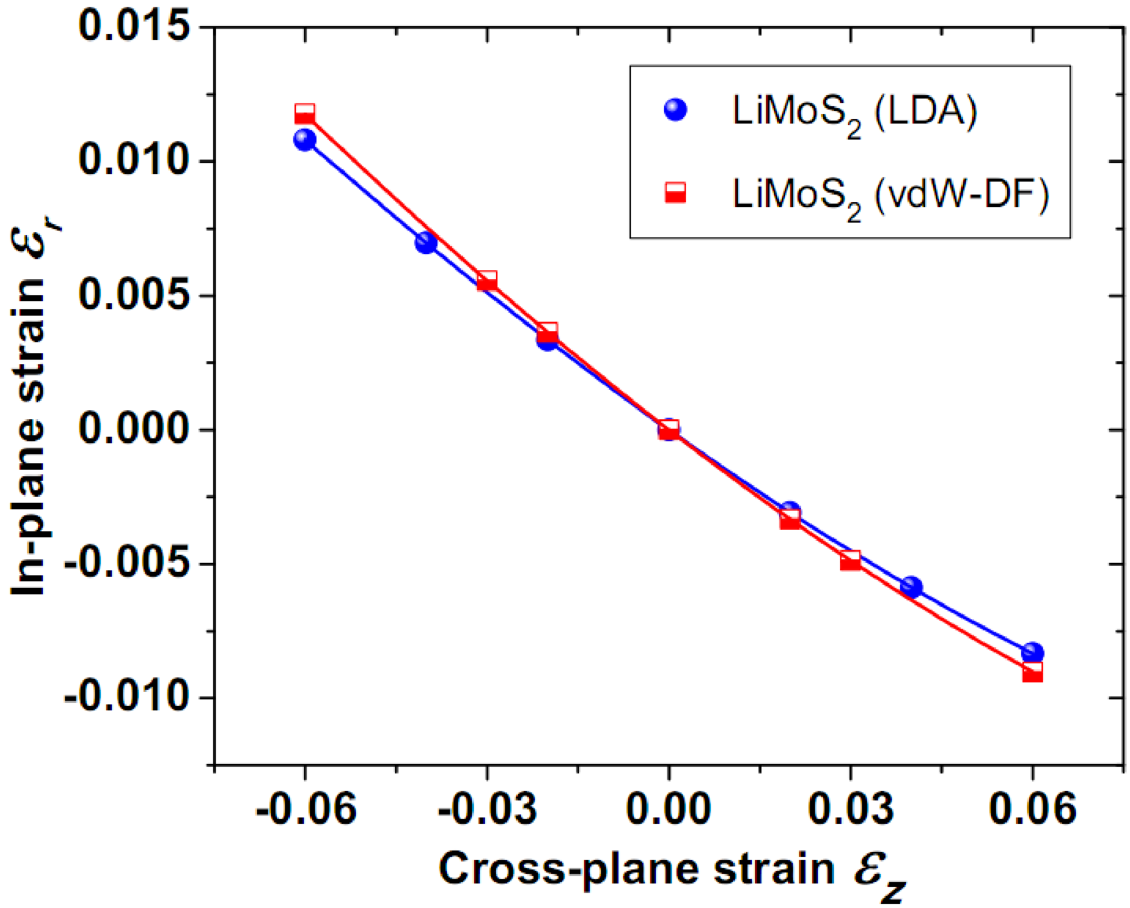

Figure S27. The Poisson's ratio as a function of cross-plane strain for $LiMoS_2$ by LDA (blue circles) and vdW-DF (red squares). In-plane strain ε_r versus cross-plane strain ε_z. Data are fitted to function $y = -\nu_1 x + \nu_2 x^2 + \nu_3 x^3$, with $\nu_1 = 0.161$ (as the linear Poisson's ratio), $\nu_2 = 0.343$ and $\nu_3 = 0.436$ for $LiMoS_2$ with LDA (blue line); $\nu_1 = 0.174$ (as the linear Poisson's ratio), $\nu_2 = 0.381$ and $\nu_3 = 0.288$ for $LiMoS_2$ with vdW-DF (red line).